PERGAMON

International Journal of Multiphase Flow 27 (2001) 1363–1396

International Journal of Multiphase Flow

www.elsevier.com/locate/ijmulflow

Bubble coalescence in turbulent flows: A mechanistic model for turbulence-induced coalescence applied to microgravity bubbly pipe flow

A.M. Kamp [a], A.K. Chesters [b], C. Colin [a,*], J. Fabre [a]

[a] *Institut de Mécanique des Fluides, UMR 5502, Avenue Camille Soula, 31400 Toulouse, France*
[b] *La Couscouillette, 11220 Montlaur, France*

Received 29 July 1999; received in revised form 21 January 2001

Abstract

A mechanistic model for bubble coalescence in turbulent flow is presented. The model is developed in two steps, which are essentially separable. In the first, expressions put forward earlier for the collision frequency and coalescence probability of equal bubbles during turbulence-driven, high-Reynolds-number collisions are extended to unequal bubbles and to take account of bubble–turbulence and bubble–bubble interactions. In the second, the resulting expression for the coalescence rate is used to derive source terms in the transport equations for the moment densities of the bubble-diameter distribution, which can readily be evaluated locally within a CFD code. The result is an extremely compact framework capable of providing predictions of the evolution of bubble size distributions in space and time at the expense of only two additional scalar transport equations. To provide an experimental validation of the model, some data on the bubble size evolution along a pipe flow under microgravity conditions have been used. Microgravity experiments on gas–liquid bubbly pipe flows have been carried out during parabolic flights in aircraft. Bubble diameter distributions have been determined from high speed video recording and image processing. In the absence of gravity, collisions between bubbles smaller than the integral length scale of turbulence are primarily due to turbulence. The results from the calculation are in good agreement with the experimental data. The model is then used to predict the influence of the void fraction, the bubble size at the pipe inlet and the liquid mean velocity on the coalescence rate.

Keywords: Bubbles; Coalescence modelling; Turbulent flow; Microgravity

* Corresponding author. Tel.: +33-5-6128-5825; fax: +33-5-6128-5810.
E-mail address: colin@imft.fr (C. Colin).

0301-9322/01/$ - see front matter
PII: S0301-9322(01)00010-6

1. Introduction

Turbulent bubbly flows occur frequently in industrial and natural systems. Important examples can be found in the petroleum, energy-producing and chemical industries. The design of such systems requires the accurate prediction of pressure drop and wall heat transfer, both of which strongly depend on the spatial distribution of the phases and on the interfacial morphology (bubble size). In gas–liquid reactors the role played by bubbles is a central one, determining the interfacial area available for mass transfer. Together with pressure variation, break-up and mass transfer, coalescence is responsible for changes in bubble sizes. The present paper will focus on the modelling of bubble growth due to coalescence in a turbulent flow, a situation for which no satisfactory modelling currently exists. This lacuna is understandable in view of the complexity of the collision and coalescence processes.

The coalescence of two bubbles can occur when they are brought together by the surrounding liquid flow or by gravitational or other body forces. The duration of such interactions is limited and coalescence will occur only if the intervening film can drain to a sufficiently small thickness to rupture in the time available. At least three sources of relative bubble motion can be distinguished:

(i) motion induced by turbulence in the continuous phase;
(ii) motion induced by mean-velocity gradients;
(iii) buoyancy (or, more generally, body-force)-induced motion, arising from different bubble slip velocities, wake interactions or helical/zigzag trajectories.

In many systems bubbles, though much larger than the Kolmogorov eddies, are smaller than the length scales of the energy-containing eddies and source (ii) is then negligible in comparison with source (i) (Appendix A). Sources (ii) and (iii), however, are generally both significant, which greatly complicates the construction and validation of coalescence models. The present study is restricted to the development of models for the contribution of turbulence to coalescence in the absence of significant body forces, which is considered an essential precursor to a more general model incorporating both turbulence and body forces.

A model is developed for bubble coalescence in the limit of high collision Reynolds numbers, [1] leading to transport equations for scalar quantities characterizing the bubble size distribution. The modelling framework is essentially that set out by Chesters (1991), generalized to take account of a distribution of bubble sizes. As transportable scalars the moments of the distribution are chosen. The considerations are worked out in detail for a log-normal distribution, for which only two moments are required and which proved adequate to describe the experimental data.

The first approximation for the collision frequency in the absence of particle slip or hydrodynamic interaction (Kuboi et al., 1972) is refined to take account of bubble slip and of the hydrodynamic interaction arising from separation-dependence of the virtual mass. The expressions for the film-drainage and bubble-interaction times put forward by Chesters (1991) are refined and extended to unequal bubbles.

An experimental validation of the model under microgravity conditions is also presented. The absence of gravity satisfies the assumption of the model, that bubble collisions are induced by velocity fluctuations due to turbulence in the liquid flow. In many practical applications, other

[1] Corresponding to a bubble cut-off diameter of around 0.5 mm in water if a cut-off Reynolds number of order 10 is taken.

bubble-collision sources exist, such as the bubble relative motion induced by mean velocity gradients in the liquid phase and differences in bubble rise velocities. A unique situation in which it is possible to isolate turbulence-induced coalescence is in bubbly flow under microgravity conditions. Drift and wake-induced collisions are nearly absent under these conditions. Likewise, mean-velocity gradients play a small role, since the velocity is almost homogeneous in the centre region of the tube, where most of the bubbles can be found (Kamp et al., 1995; Kamp, 1996). In addition, the approximation of spherical bubbles is a satisfactory one up to much larger bubble diameters.

Section 2 introduces the use of moment densities, S_γ, of the bubble-diameter distribution and their application to the practically relevant and analytically simple log-normal distribution. The transport equation for S_γ is derived and the relation examined of the coalescence source term to collision frequencies and coalescence probabilities. Section 3 then addresses the modelling of coalescence probability, determined in turn by bubble-interaction and film-drainage times. Expressions are derived for these times as a function of collision conditions and bubble-diameter ratio. Section 4 extends the expression of Kuboi et al. (1972) for collision rates to take account of slip and hydrodynamic interaction. This expression is then combined with that for coalescence probability to obtain the final expression for the coalescence source term in the transport equation for S_γ. In Section 5, the experimental data used for the validation of the model are presented. The axial evolution of bubble sizes in a turbulent bubbly pipe flow under microgravity conditions is obtained from high speed video pictures of the flow taken at the inlet and the outlet of the pipe through two visualization sections. After image processing, bubble diameter probability density functions (pdfs) at the pipe inlet and outlet are constructed. The results of the model are compared to the experimental data in Section 6. Finally a parametric study is conducted which shows how the coalescence rate in a bubbly pipe flow under microgravity conditions varies with the void fraction, the bubble size at the pipe inlet and the liquid flow rate. Conclusions and perspectives are given in Section 8.

2. Bubble-diameter distribution and transport of moment density

2.1. The approximation of a log-normal distribution

The following derivations apply to bubbly gas–liquid mixtures although similar considerations could, with minimal modifications, be applied to droplet transport. If small air bubbles are injected into a turbulent flow, coalescence leads to a non-homogeneity in the bubble sizes. The pdf for the bubble diameter, [2] d, often proves to be well represented by a log-normal distribution law although other distributions (gamma, bi-modal) have been reported as well (Piret, 1980). In what follows we assume a log-normal distribution function, but any other distribution depending on a limited number of parameters could be chosen. The pdf for diameter d is then

$$P(d) = \left(\sqrt{2\pi}\hat{\sigma}d\right)^{-1} \exp\left[-\{\ln(d/d_{00})\}^2/\left(2\hat{\sigma}^2\right)\right], \tag{1}$$

where d_{00} is a characteristic diameter and $\hat{\sigma}$ a width parameter.

[2] To allow for non-spherical bubbles d may be defined as $(6V/\pi)^{1/3}$, where V denotes the bubble volume.

The physical significance of this pdf and of the diameter d_{00} becomes clear if bubble diameters are expressed in relative rather than absolute terms. Defining a measure of relative bubble size, D, by

$$D = \ln(d/d_{00})$$

(1) becomes

$$P(d) = \left(\sqrt{2\pi}\hat{\sigma}d\right)^{-1} \exp\left[-D^2/\left(2\hat{\sigma}^2\right)\right]. \tag{2}$$

Since furthermore

$$P(d)\,\mathrm{d}(d) = P(D)\,\mathrm{d}D = P(D)\,\mathrm{d}(d)/d$$

(both the LHS and RHS representing the number of bubbles per unit volume in a given size interval), (2) yields

$$P(D) = \left(\sqrt{2\pi}\hat{\sigma}\right)^{-1} \exp\left[-D^2/\left(2\hat{\sigma}^2\right)\right]$$

corresponding to a normal distribution of D-values, with variance $\hat{\sigma}$. The maximum value of $P(D)$ is thus obtained when $D = 0$, corresponding to $d = d_{00}$. From symmetry it also follows that d_{00} represents the number-median diameter, the number of bubbles for which $d < d_{00}$ being the same as that for which $d > d_{00}$.

2.2. The transport equations for the moment densities

The volumetric number density of bubbles with diameter d is $P(d)n$, where n denotes the number of bubbles per unit volume. Ignoring bubble diffusion, the transport equation for $P(d)n$ in phase-space [3] is given by (Randolph and Larson, 1971; Achard, 1978)

$$\frac{\partial}{\partial t}[P(d)n] + \nabla \cdot [P(d)n\mathbf{v}(d)] + \frac{\partial}{\partial d}[GP(d)n] = \varphi(\mathbf{x}, d, t), \tag{3}$$

where it is assumed here that at any instant $P(d)$ depends only on one internal coordinate which is the bubble diameter, d. The "velocity" G along this internal coordinate is then a bubble growth velocity $G = \mathrm{d}(d)/\mathrm{d}t$ due to pressure variation, mass transfer, etc. $\mathbf{v}(d) = \mathrm{d}\mathbf{x}(d)/\mathrm{d}t$ is the velocity of displacement of a bubble of size d. The source or sink term $\varphi(\mathbf{x}, d, t)$ represents the contribution to $P(d)n$ of change in the number of particles, due to bubble break-up, coalescence, nucleation or collapse.

Eq. (3) implicitly assumes that n is a well-defined quantity which can be established by counting the number of bubbles present at any instant within a region which is small compared with the length scales of the flow. In turbulent flows this condition is virtually never satisfied and some kind of averaging procedure is required which must, in addition, be compatible with that applied to other variables. This is an important but difficult issue on which various approaches have been proposed. Experimentally, ensemble averaging is used to arrive at n. A consistent framework based on ensemble averaging of the two-phase equations, including the present model of coalescence, has been set out in the recent thesis of Hill (1998).

[3] A space consisting of the three spatial coordinates called "external" coordinates, together with any "internal" coordinates, such as bubble diameter, composition, etc.

Eq. (3) is a traditional Liouville–Bolzmann equation. Solving it can turn out to be a difficult job since its solutions have to be obtained in the phase space, which is essentially four-dimensional. We therefore seek a transformation which will average (2) over the internal-coordinate values and thereby reduce the dimensionality to that of a transport equation in physical space.

The γth moment density, S_γ, can be defined as

$$S_\gamma = n \int P(d) d^\gamma \, \mathrm{d}(d). \tag{4}$$

The moment densities are seen to be intensive scalar quantities which quantify the dispersion of the gas phase. Thus, S_0 is the bubble concentration $n, S_1/n$ the mean diameter, S_2 is proportional to the specific interfacial area $\alpha_i (S_2 = 4\alpha_i/\pi), S_3$ to the gas fraction $\alpha (S_3 = 6\alpha/\pi)$, etc. There is, however, no restriction to integer values of γ. As transportable scalar quantities, the moment densities have the appeal that (in the absence of changes in d or n) they are conserved during the mixing of particle (in the present case, bubble) populations. The moment densities are seen to be related to the mean diameters d_{pq}

$$d_{pq} = \frac{\int_0^\infty P(d) d^p \, \mathrm{d}(d)}{\int_0^\infty P(d) d^q \, \mathrm{d}(d)} = \left(\frac{S_p}{S_q} \right)^{1/(p-q)}, \quad p \neq q.$$

The case when $p = 3$ is particularly important

$$d_{3\gamma} = \left(\frac{S_3}{S_\gamma} \right)^{1/(3-\gamma)} = \left(\frac{6\alpha}{\pi S_\gamma} \right)^{1/(3-\gamma)}, \quad \gamma \neq 3. \tag{5}$$

The first step in the deriving the transport equations for S_γ is to multiply the terms in (3) by d^γ and integrate over all particle sizes. Since the limits of integration are independent of t and $\boldsymbol{x}$ the differential operators $\partial/\partial t$ and ∇ may be taken outside the integrals, yielding

$$\frac{\partial}{\partial t} \left\{ n \int_0^\infty P(d) d^\gamma \mathrm{d}(d) \right\} + \nabla \cdot \left\{ n \int_0^\infty P(d) \mathbf{v}(d) d^\gamma \mathrm{d}(d) \right\} + n \int_0^\infty \frac{\partial}{\partial d} \{ G(d) P(d) \} d^\gamma \mathrm{d}(d) = \varphi_\gamma(\mathbf{x}, d, t), \tag{6}$$

where ϕ_γ is a source term or a sink term due to bubble coalescence, break-up, nucleation or collapse. The second term of the LHS on (6) can be rearranged by defining a weighted average bubble velocity, $\mathbf{v}_\gamma$

$$\mathbf{v}_\gamma = \frac{\int_0^\infty P(d) \mathbf{v}(d) d^\gamma \mathrm{d}(d)}{\int_0^\infty P(d) d^\gamma \mathrm{d}(d)}.$$

Integrating by parts, the integral in the third term on the LHS of (6) becomes:

$$\int_0^\infty \frac{\partial}{\partial d} \{ G(d) P(d) \} d^\gamma \mathrm{d}(d) = G(d) P(d) d^\gamma \, |_0^\infty - \gamma \int_0^\infty P(d) G(d) d^{\gamma-1} \mathrm{d}(d).$$

For the log-normal distribution, $P(d) \to 0$ more rapidly than any power of d as $d \to 0$ or $d \to \infty$ and the first term on the RHS consequently vanishes. This will also be true of any other physically realistic pdf. Finally, defining a weighted average bubble growth velocity, G_γ

$$G_\gamma = \frac{\int_0^\infty P(d)G(d)d^\gamma \mathrm{d}(d)}{\int_0^\infty P(d)d^\gamma \mathrm{d}(d)}$$

and making use of (4), (6) can be written as

$$\frac{\partial S_\gamma}{\partial t} + \nabla \cdot \left(\mathbf{v}_\gamma S_\gamma\right) - \gamma G_{\gamma-1} S_{\gamma-1} = \varphi_\gamma. \tag{7}$$

If the source term, can be modelled, and if $\mathbf{v}_\gamma$ and G_γ are known, then (7) can be solved for S_γ.

In order to evaluate φ_γ, $P(d)$ has to be known. Since according to (1), $P(d)$ only depends on two parameters, d_{00} and $\hat{\sigma}$, it is uniquely defined by a combination of two moments S_γ. This follows from substitution of (1) in (4)

$$S_\gamma = n d_{00}^\gamma \exp(\hat{\sigma}^2\gamma^2/2). \tag{8}$$

The bubble number density can be eliminated from this equation using the fact that $S_3 = 6\alpha/\pi$ so that

$$n = \frac{6\alpha}{\pi d_{00}^3} \exp(-9\hat{\sigma}^2/2). \tag{9}$$

Combination of (8) and (9) yields

$$S_\gamma = \frac{6\alpha}{\pi} d_{00}^{\gamma-3} \exp\left\{\frac{\hat{\sigma}^2}{2}(\gamma^2 - 9)\right\}. \tag{10}$$

Thus the distribution width $\hat{\sigma}$ follows from, for example, S_1 and S_2

$$\hat{\sigma} = \left[\ln\left(\frac{6\alpha S_1}{\pi S_2^2}\right)\right]^{1/2} \tag{11}$$

and d_{00} can then be calculated by inversion of (10) once $\hat{\sigma}$ is known from (11). Hence simultaneous solution of (7) for two different values of γ, permits one to obtain the spatial variation of the pdf.

The critical issue in the use of the transport Eq. (7) is the modelling of the source term φ_γ. Below we consider the case in which φ_γ is uniquely determined by coalescence resulting from turbulence-induced bubble collisions.

2.3. Modelling of the coalescence source term

The source term φ_γ is a measure of how S_γ is modified by the coalescence of two bubbles. If a bubble with diameter d_1 coalesces with a bubble of diameter d_2, then a new bubble results with diameter $(d_1^3 + d_2^3)^{1/3}$. The decrease in S_γ due to one such coalescence process per unit volume is therefore given by

$$\Delta S_\gamma = (d_1^3 + d_2^3)^{\gamma/3} - d_1^\gamma - d_2^\gamma.$$

Denoting by $c(d_1, d_2)\,\mathrm{d}(d_1)\,\mathrm{d}(d_2)$ the number of collisions per unit time and volume of bubbles for which $d_1 \leqslant d \leqslant d_1 + \mathrm{d}(d_1)$ with bubbles for which $d_2 \leqslant d \leqslant d_2 + \mathrm{d}(d_2)$ and denoting by $P_\mathrm{c}(d_1, d_2)$ the probability that the film drainage process accompanying a collision results in coalescence, the coalescence rate (number of coalescence events per unit time and volume) is given by

$$\frac{1}{2}\int_{d_1=0}^{\infty}\int_{d_2=0}^{\infty} P_c(d_1,d_2)c(d_1,d_2)\,\mathrm{d}(d_1)\,\mathrm{d}(d_2),$$

the factor 1/2 allowing for the fact that the double integral counts each collision twice.

The source term of Eq. (7) is accordingly given by

$$\begin{aligned}\varphi_\gamma &= \frac{1}{2}\int_{d_1=0}^{\infty}\int_{d_2=0}^{\infty} P_c(d_1,d_2)\Delta S_\gamma c(d_1,d_2)\,\mathrm{d}(d_1)\,\mathrm{d}(d_2)\\ &= \frac{1}{2}\int_{d_1=0}^{\infty}\int_{d_2=0}^{\infty} P_c(d_1,d_2)\left[(d_1^3+d_2^3)^{\gamma/3}-d_1^\gamma-d_2^\gamma\right]c(d_1,d_2)\,\mathrm{d}(d_1)\,\mathrm{d}(d_2).\end{aligned} \tag{12}$$

The separation of the bubble interaction process into collision and film drainage reflects the conceptual framework usually employed to describe coalescence processes, dividing the flow into an *external* part (the flow which drives the bubbles together) and an *internal* part (the flow in the liquid film between the surfaces of the two approaching bubbles) (Coulaloglou and Tavlarides, 1977; Chesters, 1991).

The following two sections address the modelling of coalescence probability and collision rate, respectively.

3. The modelling of coalescence

3.1. Modelling approach

As a preliminary, consider the collision of equal, initially spherical, bubbles moving towards each other at equal speeds, $V/2$, along the line joining their centres in otherwise stagnant liquid in the limit of large Reynolds numbers but small Weber numbers. [4] Viscous dissipation is then minor and to the first approximation the energy of the system is conserved during the collision. At large separations bubble deformation is negligible and, neglecting the kinetic energy of the gas, that of the liquid, $C_{vm}(\rho_L \pi d^3/6)V^2$, is then constant ($\rho_L$ liquid density, C_{vm} coefficient of virtual mass). As shown in Section 3.2, C_{vm} rises from 0.5 at large separations to 0.803 at small ones and V will diminish accordingly.

At sufficiently close quarters the bubbles begin to flatten, thereby increasing their surface area and storing a corresponding proportion of the system's kinetic energy as surface free energy. An analysis of this phase of the interaction can be made if the bubble surfaces are approximated as consisting of a plane region bounded by a spherical one (Fig. 1). The interaction time, t_i, defined here as the interval between the onset of film formation and the moment at which the bubbles begin to rebound, can then be derived.

Within this picture, coalescence occurs if $t_d < t_i$, where t_d denotes the time required for film drainage from the onset of flattening to film rupture. A first approximation to t_d is provided by numerical results on film drainage for constant bubble approach velocity (Chesters and Hofman, 1982a,b), allowing an approximate expression to be derived for the ratio t_d/t_i.

[4] A situation obtainable in low-viscosity liquids for a range of d and V-values.

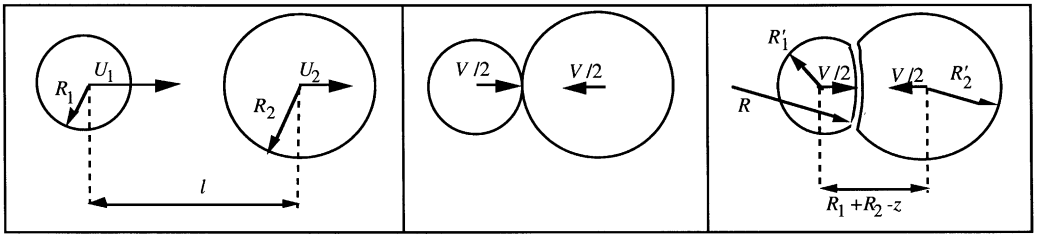

Fig. 1. Approach and deformation of two bubbles.

The following two sections extend this framework to take account of the effects of unequal bubble diameters. The resulting expression for t_d/t_i is then generalized to unrestricted Weber numbers and tested against data for bubble coalescence at a free surface. The application to the prediction of coalescence probability during turbulence-driven collisions is postponed until Section 4.2.

3.2. Interaction time

Consider a collision between bubbles of radii R_1 and R_2 moving with velocities U_1 and U_2 in the x-direction (the line joining their centres) in an unbounded liquid at rest (Fig. 1), under conditions of large collision Reynolds number but small Weber number (implying, as will be seen, that the radius of the resulting film is much smaller than the radii of the bubbles). Neglecting work done against viscous dissipation or body forces during the collision and approximating the system as isothermal, the increase in surface free energy, ΔF, accompanying deformation is balanced by a corresponding reduction in the kinetic energy of the system, $-\Delta E_k$

$$\Delta E_k + \Delta F = 0. \tag{13}$$

For an isothermal system the free energy per unit area of surface is simply the surface tension so that

$$\Delta F = \sigma \Delta A, \tag{14}$$

where σ is the surface tension and ΔA is the increase in the surface area of the bubbles due to deformation. Below, expressions are derived for E_k and ΔA as a function of bubble separation, permitting the bubble motion and resulting interaction time to be quantified.

3.2.1. Kinetic energy associated with the bubble motion

For surfactant-free systems the shear stress exerted by the bubble surface on the surrounding liquid is negligible. Neglecting viscous dissipation and confining attention for the moment to spherical bubbles, the liquid motion should then be well approximated as a potential flow. The kinetic energy of the potential flow associated with translating spheres of radii R_1 and R_2 is given by (Lamb, 1932)

$$E_k = \frac{1}{2}(LU_1^2 - 2MU_1U_2 + NU_2^2), \tag{15}$$

where the geometrical coefficients L, M and N are given by series:

$$L = \frac{2}{3}\pi\rho_L R_1^3\left\{1 + \frac{3R_1^3R_2^3}{l^3f_1^3} + \frac{3R_1^6R_2^6}{l^3f_1^3(l-f_2)^3f_3^3} + \cdots\right\}$$

$$M = 2\pi\rho_L \frac{R_1^3R_2^3}{l^3}\left\{1 + \frac{3R_1^3R_2^3}{g_1^3(l-g_2)^3} + \frac{3R_1^6R_2^6}{g_1^3g_3^3(l-g_2)^3(l-g_4)^3} + \cdots\right\}$$

$$N = \frac{2}{3}\pi\rho_L R_2^3\left\{1 + \frac{3R_1^3R_2^3}{l^3g_1^3} + \frac{3R_1^6R_2^6}{l^3g_1^3(l-g_2)^3g_3^3} + \cdots\right\}$$

with

$$f_1 = l - R_2^2/l,\ \ f_2 = R_1^2/f_1,\ \ f_3 = l - R_2^2/(l-f_2),\ \ f_4 = R_1^2/f_3,$$
$$g_1 = l - R_1^2/l,\ \ g_2 = R_2^2/g_1,\ \ g_3 = l - R_1^2/(l-g_2),\ \ g_4 = R_2^2/g_3$$

and $l(=x_1-x_2)$ the distance between the bubble centres.

Numerical evaluation of the coefficients L, M and N indicates that these tend to finite values as the sphere separation becomes small

$$L \to L_0,\ \ M \to M_0,\ \ N \to N_0 \quad \text{as } l/(R_1+R_2) - 1 \ll 1.$$

In the symmetrical case $(R_1 = R_2 = R, U_1 = -U_2 = U/2), L = N$ and (15) reduces to $E_k = (L+M)(U/2)^2$, so that $C_{vm} = 3(L+M)/4\pi R^3\rho_L$. The variation of C_{vm} with sphere separation for this case is shown in Table 1.

The insensitivity of E_k to the exact sphere separation indicates that the contribution to E_k of the flow in the narrow film between the spheres is small (even though high velocities are attained there at small separations). Since for deforming bubbles at small Weber numbers this is the only region in which the flow (and hence kinetic energy) differs from that for two spheres, it may be concluded that (15) also applies to deforming bubbles, with L, M and N approximated by their small-separation values L_0, M_0, N_0

$$E_k = \frac{1}{2}\left(L_0U_1^2 - 2M_0U_1U_2 + N_0U_2^2\right). \tag{16}$$

Table 1
Coefficient of virtual mass of equal spheres as a function of the distance, l, between their centres

$l/R-2$	C_{vm}
∞	0.5
2	0.524
1	0.559
1/2	0.608
1/4	0.660
1/8	0.705
1/16	0.740
1/32	0.764
1/128	0.790
0	0.803

The forces F_1 and F_2 (reckoned positive in the direction from bubble 1 to bubble 2), exerted by the flow on the bubbles may now be calculated from the kinetic energy via Lagrange's equations

$$F_1 = \frac{\mathrm{d}}{\mathrm{d}t}\frac{\partial E_k}{\partial U_1} - \frac{\partial E_k}{\partial x_1}, \quad F_2 = \frac{\mathrm{d}}{\mathrm{d}t}\frac{\partial E_k}{\partial U_2} - \frac{\partial E_k}{\partial x_2}.$$

For flattening bubbles, the forces F_1 and F_2 arise to counteract the deviation of the film pressure (acting as a spring, pushing the bubbles apart) from that for spheres. The sum of these forces is zero (since $\partial E_k/\partial x_2 = \partial E_k/\partial x_1$), so that

$$\frac{\mathrm{d}}{\mathrm{d}t}((L_0 - M_0)U_1 + (N_0 - M_0)U_2) = 0$$

and after integration

$$(L_0 - M_0)U_1 + (N_0 - M_0)U_2 = \text{constant} \tag{17}$$

(17) can be re-written as

$$m_1 U_1 + m_2 U_2 = (m_1 + m_2)U_0, \tag{18}$$

where

$$m_1 = \frac{L_0 N_0 - M_0^2}{N_0 - M_0}, \quad m_2 = \frac{L_0 N_0 - M_0^2}{L_0 - M_0}$$

and U_0 is a constant representing a weighted average of U_1 and U_2. Eq. (18) has the same form as the equation of conservation of momentum governing the interaction of particles of mass m_1 and m_2 and indeed for equal sized bubbles m_1 and m_2 reduce to the virtual masses ($m_1 = m_2 = L_0 + M_0$). Unlike a real mass, however, m_1 can be negative (if R_1/R_2 is less than about 0.4).

The bubble velocities can now be expressed as

$$U_1 = U_0 + \frac{m_2}{m_1 + m_2}V, \quad U_2 = U_0 - \frac{m_1}{m_1 + m_2}V,$$

where V denotes the relative velocity, $U_1 - U_2$. Substitution of these expressions into (16) yields, after re-arrangement,

$$2E_k = (L_0 - 2M_0 + N_0)U_0^2 + \frac{m_1 m_2}{m_1 + m_2}V^2$$

or

$$2E_k = (L_0 - 2M_0 + N_0)U_0^2 + \frac{L_0 N_0 - M_0^2}{L_0 - 2M_0 + N_0}V^2, \tag{19}$$

which expresses the total kinetic energy of the system as the sum of a constant term, associated with the velocity U_0, and a term associated with the relative motion of the bubbles, only the latter being available for bubble flattening. Eq. (19) differs from the corresponding equation for real interacting particles

$$2E_k = (m_1 + m_2)U_0^2 + \frac{m_1 m_2}{m_1 + m_2} V^2$$

only with regard to the coefficient of the first term. [5]

Ignoring the constant first term, (19) may be written

$$E_k = \frac{1}{2} \frac{L_0 N_0 - M_0^2}{L_0 - 2M_0 + N_0} V^2 = C_{\mathrm{vm}} \left(\frac{\rho_{\mathrm{L}} \pi}{6} \right) d_{\mathrm{eq}}^3 \left(\frac{V}{2} \right)^2, \tag{20}$$

where d_{eq} is the equivalent diameter which governs the film drainage rate (Section 3.3)

$$d_{\mathrm{eq}} = \frac{2 d_1 d_2}{d_1 + d_2}. \tag{21}$$

C_{vm} is a virtual mass coefficient defined as

$$C_{\mathrm{vm}} = \frac{L' N' - M'^2}{L' - 2M' + N'} \frac{1}{d_{\mathrm{eq}}^3}, \tag{22}$$

where

$$L' = \frac{12 L_0}{\pi \rho_{\mathrm{L}}} = d_1^3 \left(1 + \frac{3 d_2^3}{(d_1 + 2d_2)^3} + \frac{3 d_2^3}{(2d_1 + 3d_2)^3} + \mathrm{O}\left(\frac{d_1^9 d_2^9}{l^{18}} \right) \right),$$

$$M' = \frac{12 M_0}{\pi \rho_{\mathrm{L}}} = \left(\frac{251}{72} + \mathrm{O}\left(\frac{d_1^9 d_2^9}{l^{18}} \right) \right) \frac{d_1^3 d_2^3}{(d_1 + d_2)^3},$$

$$N' = \frac{12 N_0}{\pi \rho_{\mathrm{L}}} = d_2^3 \left(1 + \frac{3 d_1^3}{(2d_1 + d_2)^3} + \frac{3 d_1^3}{(3d_1 + 2d_2)^3} + \mathrm{O}\left(\frac{d_1^9 d_2^9}{l^{18}} \right) \right).$$

Table 2 presents the variation of C_{vm} with bubble diameter ratio. C_{vm} decreases monotonically with increasing d_2/d_1. The limiting result $(C_{\mathrm{vm}})_{d_2/d_1=\infty} = 1/4 (C_{\mathrm{vm}})_{d_2/d_1=1}$ can be deduced from symmetry considerations.

In the ensuing computations the terms of order $(d_1 d_2 / l^2)^9$ and higher are neglected, the resulting error being only a few percent (for bubbles of equal diameter, for example, the resulting value of C_{vm} is then 0.785, compared with the exact value of 0.803).

An expression of the available kinetic energy for bubble deformation has also been obtained by Svendsen and Luo (1996). In this study the authors have, however, only given an estimated value of the virtual mass coefficient. They found that C_{vm} is close to one for bubbles of equal diameter.

3.2.2. Increase in surface area due to bubble flattening

Provided the radius of film, a (Fig. 2) is much smaller than the radii of the bubbles (a condition satisfied, as will be seen, at small Weber numbers),

[5] As illustrated, for example, by the special case $R_1 = R_2$, for which $m_1 + m_2 = 2(L_0 + M_0)$ while $L_0 - 2M_0 + N_0 = 2(L_0 - M_0)$.

Table 2
Diameter-ratio dependence of the coefficient of virtual mass in the limit of small sphere separation

d_2/d_1	C_{vm}
1	0.803
1.09	0.796
1.19	0.775
1.41	0.704
2	0.539
4	0.341
16	0.231
256	0.203
∞	0.201

$$a \ll R_i, \quad i = 1, 2 \tag{23}$$

the centre surface of the film is spherical with radius of curvature, R, given by

$$R = \frac{2R_1'R_2'}{R_1' - R_2'}$$

(Abid and Chesters, 1994: though for interacting drops, the derivation is equally applicable to bubbles). The primes serve to distinguish the instantaneous bubble radii (which must increase slightly during deformation in order to conserve bubble volume) from their initial values, R_1 and R_2. If the thickness of the film is neglected and the bubbles approximated as spherical outside the film, expressions for the increases in bubble surface area, ΔA_1 and ΔA_2, as a function of the

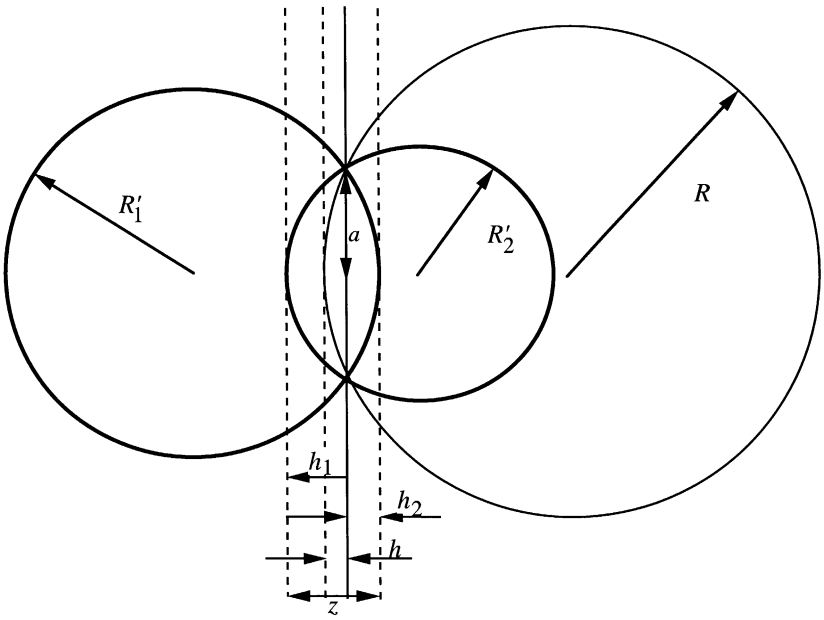

Fig. 2. Collision of bubbles with radii R_1 and R_2.

distance between their centres, $R_1 + R_2 - z$, may be derived from simple geometrical considerations, making use of (23):

$$\Delta A_1 \approx 4\pi\left(R_1'^2 - R_1^2 - \frac{z}{4(R_1+R_2)}(R_1R - R_2R - 2R_1'R_2)\right),$$

$$\Delta A_2 \approx 4\pi\left(R_2'^2 - R_2^2 - \frac{z}{4(R_1+R_2)}(R_1R - R_2R - 2R_1'R_1)\right).$$

The values of R_1' and R_2' follow from volume conservation:

$$\frac{4}{3}\pi R_1^3 = \frac{4}{3}\pi\left[R_1'^3 - \frac{h_1^2}{4}(3R_1' - h_1) - \frac{h^2}{4}(3R - h)\right],$$

$$\frac{4}{3}\pi R_2^3 = \frac{4}{3}\pi\left[R_2'^3 - \frac{h_2^2}{4}(3R_2' - h_2) + \frac{h^2}{4}(3R - h)\right],$$

where h_1, h_2 and h are defined in Fig. 2 ($h_1 + h_2 = z$). Elimination of R_1' and R_2' now gives:

$$\Delta A_1 = \Delta A_2 = \frac{\pi z^2}{4}, \quad \Delta A = \frac{\pi z^2}{2}. \tag{24}$$

Since the film radius a is related to z as $z = a^2/R_{eq}$ (with $d_{eq} = 2R_{eq}$ given by (21)), (24) can also be written as

$$\frac{\Delta A}{A_{eq}} = \frac{\Delta A}{8\pi R_{eq}^2} = \left(\frac{a}{2R_{eq}}\right)^4$$

indicating that for unequal bubbles ΔA is the same as for equal bubbles of radius R_{eq}. Substitution of (24) in (14) now gives

$$\Delta F \approx \pi\sigma\frac{z^2}{2}. \tag{25}$$

3.2.3. Equation of motion

The energy conservation equation (13) during the collision process yields

$$E_{k0} = E_k + F,$$

E_{k0} being the initial kinetic energy for the bubbles at the moment that their surfaces first touch. Combination of (20) and (25) with (13) now yields

$$V = \frac{\mathrm{d}z}{\mathrm{d}t} = V_0\left(1 - \frac{12\sigma z^2}{\rho_L C_{vm} d_{eq}^3 V_0^2}\right)^{1/2}, \tag{26}$$

V_0 being the relative velocity of the bubbles at the onset of deformation. As a first approximation the interaction time, t_i, is defined as the interval between the moment at which the bubbles touch ($z = 0$) and that at which they begin to separate (corresponding to $\mathrm{d}z/\mathrm{d}t = 0$). Integration of Eq. (26) then gives

$$t_i = \frac{\pi}{4}\left(\frac{\rho_L C_{vm} d_{eq}^3}{3\sigma}\right)^{1/2}, \tag{27}$$

in which C_{vm} is given by (22).

3.3. Drainage time

The problem of film drainage between two colliding bubbles has been extensively investigated for the case where the Weber number based on the equivalent diameter and the relative velocity V_0 is much smaller than unity (Lee and Hodgson, 1968; Kirkpatrick and Lockett, 1974; Chesters and Hofman, 1982b; Heng-Kwong and Koch, 1994)

$$We_{eq} = \frac{\rho_L V_0^2 d_{eq}}{2\sigma} \ll 1.$$

Chesters and Hofman obtained numerical solutions for the case of constant approach velocity. After flattening a dimple is formed, the location of the minimum film thickness, h_{min}, moving radially outward with time, while the drainage rate, $-\mathrm{d}h_{min}/\mathrm{d}t$, stabilizes at a constant value of the order of 10% of the bubble approach velocity. Even without taking account of the de-stabilizing effects of van der Waals forces in the final stages of drainage, the drainage time t_d is thus predicted to be finite. The results show that t_d varies as $\rho_L V_0 d_{eq}^2/\sigma$. For a given diameter ratio, t_i varies as $(\rho_L d_{eq}^3/\sigma)^{1/2}$ and t_d/t_i consequently varies as $(We_{eq})^{1/2}$.

Two problems arise in using these results to obtain an expression for the drainage time t_d. The first is that the approach velocity is not in reality constant, as discussed in the preceding section. For sufficiently small Weber numbers, however, the approximation of constant approach velocity is acceptable since $t_d \ll t_i$ and drainage is consequently completed before the approach velocity has diminished significantly.

The second problem concerns the choice of "the onset" of film drainage. A definition consistent with the analysis of the interaction time t_i (Section 3.2) would be the onset of flattening. However, in contrast with the simplified model used to derive t_i, a sharp onset of flattening is not present in reality. Rather, a gradual increase occurs from negligible deformation at large bubble separations to complete flattening when the pressure at the film centre attains the value of $4\sigma/d_{eq}$. Somewhat arbitrarily, therefore, the onset of drainage is defined, following Chesters (1991), as the moment at which the pressure in the film equals $2\sigma/d_{eq}$, which is half of the pressure required to obtain complete film flattening. This corresponds to a transformed film minimum thickness, $h_{min}^* = (2h_{min}/d_{eq}We_{eq})$ of about 0.13. The ensuring transformed time required for h_{min}^* to become zero is then is found to be $t_d^* = 2t_d V_0/d_{eq}We_{eq} \approx 0.5$. In a dimensional representation, the drainage time between two bubbles of diameters d_1 and d_2 is thus given by

$$t_d = \frac{\rho_L V_0 d_{eq}^2}{8\sigma}. \tag{28}$$

It can be shown (Chesters, 1991) that the viscous forces in the gas can be neglected during all but the very last stages of the process. Like van der Waals forces, the influence of these forces on the drainage time should then be minor, since the last stages of drainage occur extremely rapidly.

From (28) and (27), the ratio of the drainage time and the interaction time in the small Weber number limit is given by

$$\frac{t_d}{t_i} \approx \frac{1}{2\pi}\left(\frac{3\rho_L V_0^2 d_{eq}}{C_{vm}\sigma}\right)^{1/2} \approx \frac{1}{2\pi}\left(\frac{6We_{eq}}{C_{vm}}\right)^{1/2}, \tag{29}$$

where C_{vm} is a function of d_1/d_2 given by (22).

Eq. (29) is now generalized to any Weber number

$$\frac{t_d}{t_i} = \frac{k_1}{2\pi}\left(\frac{3\rho_L V_0^2 d_{eq}}{C_{vm}\sigma}\right)^{1/2}, \tag{30}$$

where the correction factor k_1, which takes account both of the effect of finite Weber number and of the various approximations made in deriving the expressions for t_d and t_i, is expected to be of order 1. The coalescence probability, P_c is then given by

$$P_c(t_d/t_i) = \begin{cases} 0 & \text{if } t_d/t_i > 1, \\ 1 & \text{if } t_d/t_i < 1. \end{cases} \tag{31}$$

A first check on (30) is provided by recent data on the coalescence of bubbles at a free surface in highly purified water (Duineveld, 1994), which indicates that bubbles of radius 0.337 mm or more bounce one or more times before coalescing. The value of k_1 implied by this result is obtained by setting the RHS of (30) equal to unity, taking $d_1 = 2 \times 0.337$ mm and $d_2 = \infty$. As $d_2 \to \infty, d_{eq} \to 2d_1, C_{vm} \to 0.201$ (see Table 2) and (30) thus yields

$$\frac{k_1}{2\pi}\sqrt{\frac{6\rho_L V_0^2 d_1}{0.201\sigma}} = \frac{k_1}{2\pi}\sqrt{\frac{6We_{eq}}{0.201}} = 1. \tag{32}$$

The rise velocity, U_∞, of bubbles of radius 0.337 mm follows from the approximate relation for the drag coefficient, C_D (Moore, 1963)

$$C_D \cong \frac{48}{Re}\left(1 - \frac{2.21}{Re^{1/2}}\right), \quad Re = \frac{\rho_L d_1 U_\infty}{\mu_L}$$

from which it is deduced that $We_{eq} \cong 0.24$, if V_0 is equated [6] with U_∞. (32) now yields $k_1 \approx 2.5$, which is indeed of order unity.

[6] In reality, V_0 (the final velocity of approach, just prior to flattening) will be somewhat smaller than U_∞ since C_{vm} increases as the free surface is approached. In the present case, however, this effect will be partially offset by the buoyancy which will no longer be fully compensated by drag. No attempt is made here to refine the approximation $V_0 \approx U_\infty$. Gravity will likewise influence the subsequent deformation and drainage process to some extend. It can, however, be shown that such effects are minor for a bubble of the size concerned here.

4. Collision and coalescence rates

4.1. Collision rate

As noted in Section 1, bubbles in two-phase systems involving low-viscosity liquids are generally much larger than the Kolmogorov eddies yet smaller than the (Eulerian integral) length scales of the energy-containing eddies. The collision between bubbles is then typically dominated by turbulence rather than mean-velocity gradients (see Appendix A). Before focussing on turbulence-induced collisions, we note that under certain circumstances bubbles have been found to become entrapped in vortex structures, leading to higher local concentrations which favour collisions. In Appendix B we show that such effects should not occur in the present experimental studies (nor were they observed) and are not to be expected in most practical systems.

If a collision is defined as a contact which would occur were the bubbles not to deform and if the bubble centres are supposed to follow the undisturbed flow, then the collision frequency can be found from statistical considerations analogous to those used in the kinetic theory of gases applied to turbulent motions in the inertial subrange. Using this approach Kuboi et al. (1972) arrived at an expression for the number of collisions of equal particles per unit time and volume, which they found to agree satisfactorily with visual observations of collision rates in dilute turbulent emulsions

$$C = \left(\frac{8\pi}{3}\right)^{1/2} n^2 d^2 V_t, \tag{33}$$

where V_t is a turbulence velocity scale $V_t = (\varepsilon d)^{1/3}$, providing a measure of the relative velocity of two material points in the liquid a distance d apart and ε is the rate of dissipation of the turbulent kinetic energy per unit mass (Hinze, 1975).

To extend the relationship (33) to a distribution of bubble sizes, we assume first that m distinct bubble sizes exist, each occurring n_i times: $n_1 + n_2 + \cdots + n_m = n$. Eq. (33) can then be extended to

$$C = \left(\frac{8\pi}{3}\right)^{1/2} \sum_{k=1}^{m} \sum_{l=1}^{m} n_k n_l \left(\frac{d_k + d_l}{2}\right)^2 V(d_k, d_l),$$

where

$$V(d_k, d_l) = \left(\varepsilon \frac{d_k + d_l}{2}\right)^{1/3}. \tag{34}$$

Converting this expression to a continuous distribution of bubble sizes by the transformation $n_k = nP(d_k)$ we obtain a total collision rate

$$C = \frac{1}{2} \int_{d_1=0}^{\infty} \int_{d_2=0}^{\infty} c(d_1, d_2)\, \mathrm{d}(d_1)\, \mathrm{d}(d_2),$$

where

$$c(d_1, d_2) = 2\left(\frac{8\pi}{3}\right)^{1/2} n^2 P(d_1) P(d_2) \left(\frac{d_1 + d_2}{2}\right)^2 V(d_1, d_2). \tag{35}$$

$V(d_1, d_2)$ is a measure of the relative velocity of two material points in the liquid a distance $d_1 + d_2$ apart. In general, a bubble accelerates faster than the liquid which induces the fluctuation. The ratio between the dispersed phase velocity fluctuations and the continuous phase velocity fluctuations is indicated by the coefficient C_t (see for example Eppinger, 1995; Deutsch, 1992). A second correction to $V(d_1, d_2)$ arises from the deceleration of the bubbles as they approach each other closely due to an increase in their coefficient of virtual mass. Neglecting viscous dissipation, the kinetic energy of the bubbles remains constant. Denoting the relative velocity at close proximity by V_0 and that at large separation by V_∞, conservation of the kinetic energy leads to $(C_{vm})_0 V_0^2 = (C_{vm})_\infty V_\infty^2$. For two bubbles of equal diameter, $(C_{vm})_0 = 0.803$ (see Table 1) while $(C_{vm})_\infty = 0.5$, yielding $(C_{vm})_0/(C_{vm})_\infty = 1.61, V_\infty/V_0 = \sqrt{1.61}$. For the opposite extreme case of a bubble approaching a plane interface $(d_2/d_1 \to \infty)$ both $(C_{vm})_0$ and $(C_{vm})_\infty$ are a factor 4 smaller (see Table 2), once more yielding $V_\infty/V_0 = \sqrt{1.61}$. For intermediate d_2/d_1 the factor $\sqrt{1.61}$ also constitutes a reasonable approximation. Thus, correcting $V(d_1, d_2)$ for these effects, (34) is replaced by [7]

$$V(d_1, d_2) = \frac{C_t}{\sqrt{1.61}} \left(\varepsilon \frac{d_1 + d_2}{2} \right)^{1/3} \tag{36}$$

and (35) by:

$$c(d_1, d_2) = 2\sqrt{\frac{8\pi}{3}} \left(\frac{6\alpha}{\pi d_{30}^3} \right)^2 \frac{C_t \varepsilon^{1/3}}{\sqrt{1.61}} \frac{1}{2\pi\hat{\sigma}^2 d_1 d_2} \exp\left[-\left(\left(\mathrm{Ln}\left(\frac{d_1}{d_{00}} \right) \right)^2 + \left(\mathrm{Ln}\left(\frac{d_2}{d_{00}} \right) \right)^2 \right) \Big/ 2\hat{\sigma}^2 \right] \left(\frac{d_1 + d_2}{2} \right)^{7/3}, \tag{37}$$

where the bubble number density n has been eliminated with the help of the relation

$$n = 6\alpha/(\pi d_{30}^3).$$

4.2. Coalescence rate

Eq. (30) provides an expression for t_d/t_i in the case of frontal collisions (relative-velocity vector directed along the line joining the bubble centres). In this case the coalescence probability changes abruptly from 1 for collisions in which $t_d/t_i < 1$ to 0 for those in which $t_d/t_i > 1$, as illustrated by the case of bubbles rising to a free surface. In the case of turbulence-driven collisions a typical value for V_0 will be given by (36)

$$V_0 = k_2 V(d_1, d_2) = \frac{k_2 C_t}{\sqrt{1.61}} \left(\epsilon \frac{d_1 + d_2}{2} \right)^{1/3}, \tag{38}$$

where k_2 is of order unity. Insertion of (38) in (30) now yields a typical value of the ratio t_d/t_i during a turbulence-driven collision

[7] In multiplying $V(d_1, d_2)$ by a factor C_t we implicitly assume that the bubble–turbulence field is a replica of the liquid–turbulence field aside from a scaling factor of C_t. In reality this will not be so and the scaling factor for relative velocities over a length scale $(d_1 + d_2)/2$ may be either greater or smaller than C_t. In the absence of information on this subject we take a scaling factor of C_t as the best first approximation.

$$\frac{t_d}{t_i} = \frac{k_1 k_2 C_t}{2\pi\sqrt{1.61}} \left(\varepsilon \frac{d_1 + d_2}{2}\right)^{1/3} \left(\frac{3\rho_L d_{eq}}{C_{vm}\sigma}\right)^{1/2}. \tag{39}$$

Individual values of V_0 will vary within a given-ε environment. In addition, collisions will not in general be frontal, the angle between the relative-velocity vector and the line joining the bubble centres varying from one collision to another. As a consequence the coalescence probability will not change abruptly as t_d/t_i passes the value of unity but vary smoothly from almost unity when $t_d/t_i \ll 1$ to almost zero when $t_d/t_i \gg 1$. Instead of attempting a theoretical derivation of P_c, we will follow a semi-empirical approach and choose P_c as an exponential probability function of the ratio between t_d and t_i (Coulaloglou and Tavlarides, 1977; Ross, 1971)

$$P_c \approx \exp(-t_d/t_i). \tag{40}$$

Combination of (39) and (40) now yields, after rearrangement,

$$P_c = \exp\left[-K_p\sqrt{We_{00}}\left(\frac{d_1^* d_2^*}{C_{vm}}\right)^{1/2}\left(\frac{d_1^* + d_2^*}{2}\right)^{-1/6}\right], \tag{41}$$

where

$$We_{00} = \frac{\rho_L[(\varepsilon d_{00})^{1/3} C_t/\sqrt{1.61}]^2 d_{00}}{2\sigma}, \quad d_i^* = \frac{d_i}{d_{00}}, \quad K_p = \frac{\sqrt{6}k_1 k_2}{2\pi}. \tag{42}$$

After substitution of $c(d_1, d_2)$ and P_c in (12), the source term φ_γ of the transport equation of the moments S_γ of the pdf of bubbles diameters may be calculated

$$\varphi_\gamma = K_c\sqrt{\frac{8\pi}{3}}\left(\frac{6\alpha}{\pi}\right)^2 \frac{C_t \varepsilon^{1/3} d_{00}^{\gamma+7/3}}{\sqrt{1.61} d_{30}^6} \frac{I(\gamma, \hat{\sigma}, d_{00})}{2\pi\hat{\sigma}^2}(2^{\gamma/3} - 2), \tag{43}$$

where K_c is a constant of order 1 which takes into account the approximations which have been made in the derivation of the model. $I(\gamma, \hat{\sigma}, d_{00})$ denotes the double integral over all bubbles sizes of the terms which depend on d_1^* and d_2^*

$$I(\gamma, \hat{\sigma}, d_{00}) = \int_{d_1^*=0}^{\infty}\int_{d_2^*=0}^{\infty}\left((d_1^{*3} + d_2^{*3})^{\gamma/3} - d_1^{*\gamma} - d_2^{*\gamma}\right)\left(\frac{d_1^* + d_2^*}{2}\right)^{7/3} P_{00}^b \times \frac{e^{-\left((\ln d_1^*)^2 + (\ln d_2^*)^2\right)/2\hat{\sigma}^2}}{d_1^* d_2^* (2^{\gamma/3} - 2)} \, d(d_1^*)\, d(d_2^*),$$

where

$$b = \sqrt{d_1^* d_2^*}\left(\frac{d_1^* + d_2^*}{2}\right)^{-1/6}\sqrt{\frac{(C_{vm})_{d_1=d_2}}{C_{vm}}}$$

and P_{00} is a characteristic probability of coalescence (the value of P_c when $d_1 = d_2 = d_{00}$)

$$P_{00} = \exp\left(-K_p\sqrt{\frac{We_{00}}{(C_{vm})_{d_1=d_2}}}\right). \tag{44}$$

The diameters d_{00} and d_{30} can be eliminated from (43). Namely, from (5), the following relation can be obtained

$$d_{00}^{\gamma+7/3} d_{30}^{-6} = \left(\frac{6\alpha}{\pi S_\gamma}\right)^{\gamma-11/3/3-\gamma} \mathrm{e}^{-\frac{\hat{\sigma}^2}{2}(\gamma^2-2/3\gamma+7)}.$$

Then Eq. (43) becomes

$$\varphi_\gamma = K_c \sqrt{\frac{8\pi}{3}} \left(\frac{6\alpha}{\pi}\right)^{7/3-\gamma/3-\gamma} \frac{C_t \varepsilon^{1/3}}{\sqrt{1.61}} (2^{\gamma/3}-2) f(\gamma, \hat{\sigma}, P_{00}) S_\gamma^{11/3-\gamma/3-\gamma} \tag{45}$$

with

$$f(\gamma, \hat{\sigma}, P_{00}) = \frac{I(\gamma, \hat{\sigma}, d_{00})}{2\pi\hat{\sigma}^2} \mathrm{e}^{-\frac{\hat{\sigma}^2}{2}(\gamma^2-2\gamma/3+7)}.$$

In the limit $\hat{\sigma} \to 0, b \to 1$ and $f(\gamma, \hat{\sigma}, P_{00}) \to P_{00}$ for all γ. In Fig. 3, $f(\gamma, \hat{\sigma}, P_{00})$ is plotted for several values of $\hat{\sigma}$ and for $\gamma = 1, \gamma = 2$ and $\gamma = 4$. The approximation $f = P_{00}$ is seen to be a good one only for $\hat{\sigma} < 0.1$. For $\hat{\sigma} < 0.3$, $f(\gamma, \hat{\sigma}, P_{00})$ is well fitted by a power law

$$f(\gamma, \hat{\sigma}, P_{00}) = g_\gamma(\hat{\sigma}) P_{00}^{c_\gamma(\hat{\sigma})}, \tag{46}$$

where $g_\gamma(\hat{\sigma})$ and $c_\gamma(\hat{\sigma})$ are quadratic functions of $\hat{\sigma}$ whose coefficients are given in Table 3. For $\hat{\sigma} > 0.3$, (46) may also be used provided $P_{00} > 0.01$.

Making use of (45) and (46), the transport Eq. (7) can be numerically solved for two moments of the bubble diameter distribution, for example S_1 and S_2. From these two moments d_{00} and $\hat{\sigma}$ may then be calculated using (10) and (11)

$$d_{00} = \frac{6\alpha}{\pi S_2} \mathrm{e}^{-5\hat{\sigma}^2/2}, \quad \hat{\sigma} = \sqrt{\ln\left(\frac{6\alpha S_1}{\pi S_2^2}\right)} \tag{47}$$

and the space-time evolution of the pdf of the bubble diameter determined. In this way it is possible, solving only for the transport of two moments of the pdf of bubble diameters, to obtain its space-time variation. Using classical population balance methods, a far greater number of equations would have to be solved.

Note that the model still contains two undetermined constants (K_c and K_p) of order 1, which reflect the approximations made in the modelling of the collision rate and the coalescence probability. These parameters will be determined experimentally in the next section by comparison of numerical simulation results with the set of experimental data obtained under microgravity conditions.

5. Experiments on microgravity bubbly pipe flow

5.1. Description of the experimental device

Experiments were performed with the two-phase flow loop EDIA (Colin et al., 1991), under microgravity conditions during parabolic flights aboard the Caravelle "ZERO-G" aircraft.

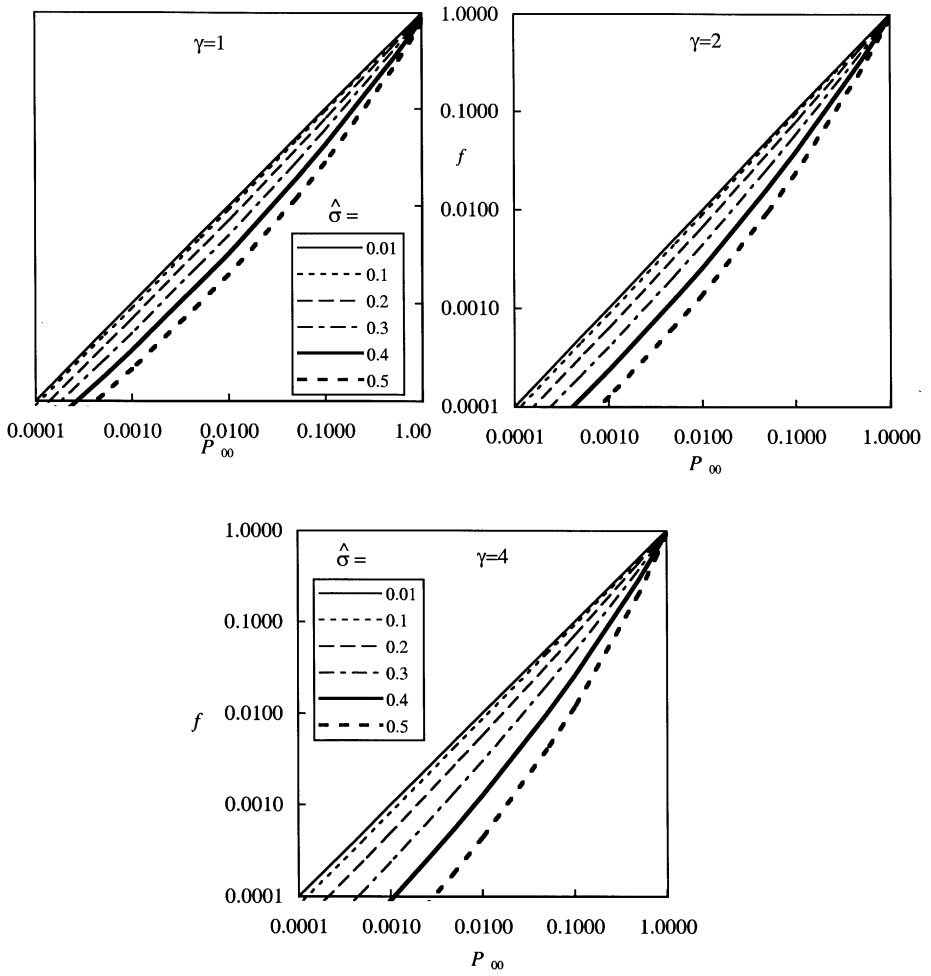

Fig. 3. Values of the function f for $\gamma = 1, \gamma = 2$ and $\gamma = 4$.

During each parabolic flight, 30 periods of approximately 20 s of microgravity conditions were obtained during which the level of residual acceleration experienced by the flowing fluids is less than $3 \times 10^{-2}g$, where g is the acceleration due to earth gravity. The measurements are performed during these periods, after a waiting time which guarantees establishment of the flow.

The principal part of the installation consists of a $D = 40$ mm diameter, 4 m long transparent Plexiglas pipe. The pipe is equipped with two visualization sections, one at a distance X_i from the bubble injection point, and the other at a distance L from the first visualization section (see Table 4). These visualization sections are rectangular boxes filled with water and serve to reduce parallax errors in flow visualizations. Flow pictures are taken through the visualization sections with two synchronized high-speed video cameras (Kodak Ektapro EM), operating at 1000 frames/second. During the flights, pictures are recorded on SVHS videotapes. After the flights, the video recordings are digitized by an A/D board and stored on the hard disk of a microcomputer PC486. In spite of the use of visualizing boxes, a small distortion of the pictures

Table 3
Values of the coefficients g_γ and c_γ used in (46)

$f(\gamma,\hat{\sigma},P_{00})=g_\gamma P_{00}^{c_\gamma}$ with	$g_\gamma=1+g'_\gamma\hat{\sigma}+g''_\gamma\hat{\sigma}^2$		$c_\gamma=1+c'_\gamma\hat{\sigma}+c''_\gamma\hat{\sigma}^2$	
	g'_γ	g''_γ	c'_γ	c''_γ
$\gamma=1$	−0.0531	−0.6283	0.0374	1.3936
$\gamma=2$	−0.0411	−0.2524	−0.0148	1.9383
$\gamma=4$	−0.0254	−0.2528	−0.0499	3.0813

remains. For a rigorous calibration, a calibration grid is located inside the water-filled tube and filmed by the two cameras.

Air is injected at the inlet of the pipe through 8 peripheral holes of 1 mm diameter located at the 20 mm i.d. nozzle of a venturi. A conductivity probe made of two stainless steel flush-mounted rings inside the pipe wall located near the outlet of the tube is used to measure the cross-sectional averaged void fraction α. The pressure drop ΔP over two lengths of the tube is measured with two Validyne pressure transducers.

5.2. Operating conditions

During several flight campaigns bubble size measurements were obtained (Colin, 1990) under different experimental conditions. These conditions are represented in Table 4, including: an identifier for each run (D16–I18), the distance X_i between the bubble injection point and the first visualization section, the distance L between the first visualization section and the second, the liquid and gas superficial velocities j_L and j_G, the cross-sectional averaged void fraction α, and the pressure gradient dp/dz.

Table 4
Flow parameters

Run	X_i (m)	L (m)	j_L (m/s)	j_G (m/s)	α	$-dp/dz$ (Pa/m)
D16	0.65	2.86	0.888	0.051	0.0412	226
D18	0.65	2.86	0.881	0.129	0.0948	270
D21	0.65	2.86	1.558	0.061	0.0286	566
D24	0.65	2.86	1.521	0.129	0.0595	580
D3	0.65	2.86	0.331	0.035	0.0902	35
E14	0.65	2.86	0.956	0.05	0.0407	240
E16	0.65	2.86	0.954	0.128	0.0912	273
E17	0.65	2.86	0.937	0.219	0.15	248
E23	0.65	2.86	1.562	0.064	0.0356	552
E24	0.65	2.86	1.548	0.126	0.0643	570
E7	0.65	2.86	0.489	0.047	0.0688	88
G17	0.48	3.2	0.96	0.037	0.033	265
G29	0.48	3.2	0.76	0.134	0.119	216
G26	0.48	3.2	0.85	0.05	0.0462	252
G21	0.48	3.2	0.89	0.11	0.0869	306
I17	0.48	3.2	0.862	0.124	0.092	236
H23	0.48	3.2	0.833	0.165	0.14	259
I18	0.48	3.2	0.842	0.223	0.17	221

5.3. Experimental results

Some visualizations of the flow are presented in Fig. 4, showing the magnitude of the coalescence rate in microgravity. As reported by Colin et al. (1991), a much stronger coalescence is obtained under microgravity conditions than those found in laboratory conditions for the same flow rates.

Bubble diameters at the inlet section are between 2 and 5 mm and decrease as the liquid flow rate increases, due to an increase of the drag force acting on the growing bubbles, which is favourable to bubble detachment. The bubble size grows along the pipe due to bubble coalescence.

Applying different image processing operations (threshold, outline closure, identification of the different bubbles), the projected area A_i of each bubble i is determined and an average diameter d_i of the bubble is calculated $d_i = \sqrt{4A_i/\pi}$ (Bongiovanni, 1996). Using the ensemble of detected bubble sizes, an experimentally obtained distribution $P_e(d)$ of the bubble diameters can be determined at the inlet and outlet visualization sections. These distributions are plotted in Fig. 5 for four different runs. Least mean square fits by log-normal laws (1) are also given.

The error Err due to the fitting of the experimental pdf $P_e(d)$ by a log-normal law $P(d)$ is estimated as follows:

$$\mathrm{Err} = \sqrt{\sum_{i=1}^{p} \left(P_e(d_{i+1/2})\Delta d - \int_{d_i}^{d_{i+1}} P(d)\,\mathrm{d}(d) \right)^2}, \tag{48}$$

where p is the number of classes of the experimental pdf, Δd is the width of each class ($=1$ mm), $P_e(d_{i+1/2})$ is the percentage of bubbles with diameters between d_i and d_{i+1}.

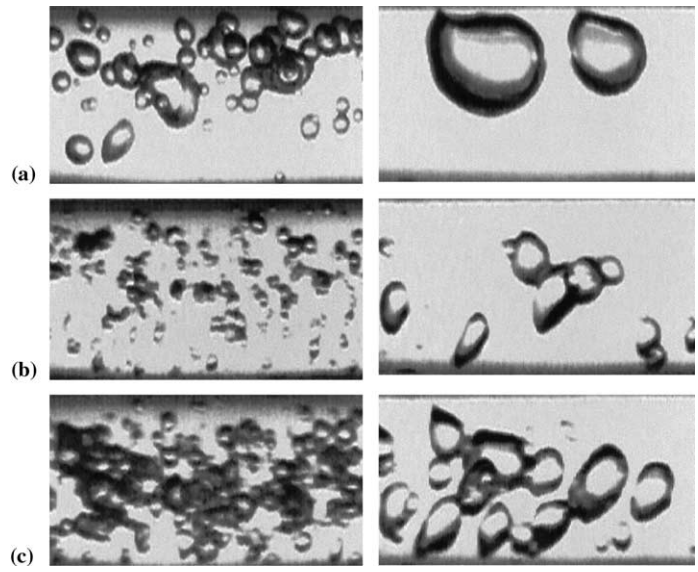

Fig. 4. Flow visualization at the pipe inlet (left) and outlet (right): digitized pictures: (a) Run D3: $j_L = 0.33$ m/s, $\alpha = 0.09$; (b) Run E14: $j_L = 0.96$ m/s, $\alpha = 0.04$; (c) Run E16: $j_L = 0.95$ m/s, $\alpha = 0.09$.

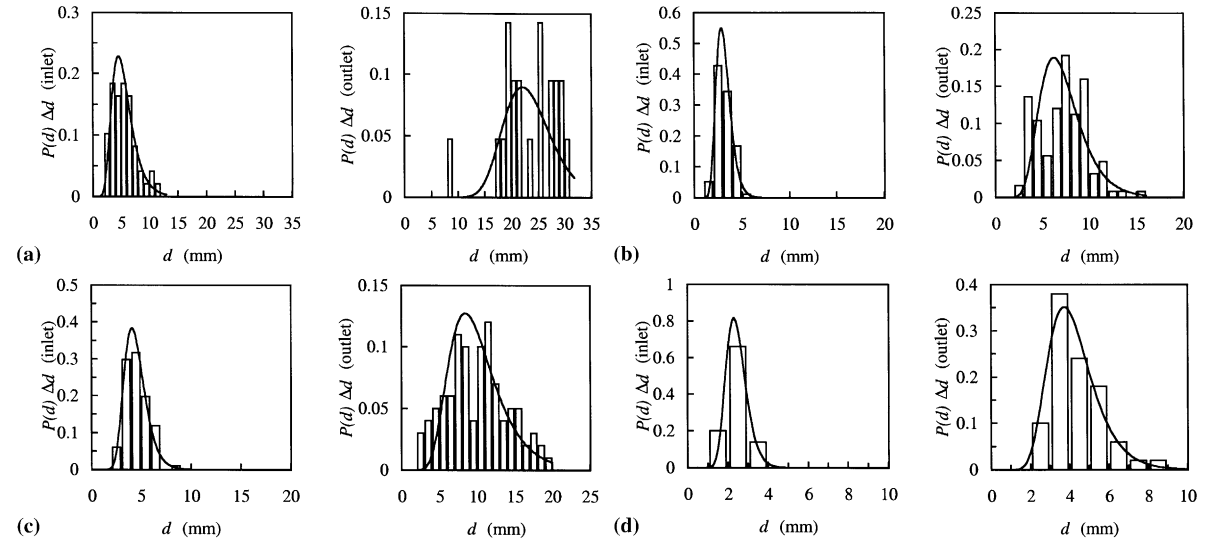

Fig. 5. Pdf of the bubbles diameters at the pipe inlet (left) and outlet (right): (a) Run D3: $j_L = 0.33$ m/s, $\alpha = 0.09$; (b) Run E14: $j_L = 0.96$ m/s, $\alpha = 0.04$; (c) Run E16: $j_L = 0.95$ m/s, $\alpha = 0.09$; (d) Run D21: $j_L = 1.56$ m/s, $\alpha = 0.03$.

The agreement between the log-normal distribution $P(d)$ and the experimentally obtained distribution $P_e(d)$ is reasonably good, taking into account the limited amount of bubbles available for the determination of $P_e(d)$. The relatively poor agreement for the experiments D3 and E7 is explained by the fact that the measurements are based on very few bubbles in these cases (see Tables 5 and 6 and Fig. 5). The good agreement in the other cases supports the hypothesis made in the theoretical model, that the pdf of particle sizes can be well represented by a log-normal law.

The detected bubble sizes can also be used to determine several characteristic diameters $d_{\gamma\delta}$ of a population of k bubbles

$$d_{\gamma\delta} = \left(\frac{\sum_{i=1}^{k} d_i^{\gamma}}{\sum_{i=1}^{k} d_i^{\delta}} \right)^{1/\gamma-\delta}. \tag{49}$$

The number of bubbles k required to calculate the characteristics diameters d_{10}, d_{20}, d_{30} and d_{32} is fixed by an arbitrary convergence criteria of $\pm 2\%$

$$\frac{| d_{\gamma\delta}(k+10) - d_{\gamma\delta}(k) |}{d_{\gamma\delta}(k)} \leqslant 0.02. \tag{50}$$

The greatest value of k is required for the convergence of the Sauter diameter d_{32}.

The parameters d_{00} and $\hat{\sigma}$ can be calculated from the mean volumetric diameter d_{30} and the Sauter diameter d_{32}:

$$d_{00} = d_{30} \exp\left(-\frac{3}{2} \ln\left(\frac{d_{32}}{d_{30}} \right) \right), \quad \hat{\sigma} = \sqrt{\ln\left(\frac{d_{32}}{d_{30}} \right)}. \tag{51}$$

Note that the values of the different characteristic diameters are averaged across the pipe sections.

The results that are obtained by application of Eqs. (48)–(51) at the inlet section are presented in Table 5, and those obtained at the outlet section in Table 6: number k of bubbles required for the convergence of d_{32}, the different diameters d_{10}, d_{30}, d_{32}, the r.m.s. values σ_{10}, σ_{30} of the mean

Table 5
Bubble diameters at pipe inlet

Run	k	d_{10} (mm)	σ_{10} (mm)	d_{30} (mm)	σ_{30} (mm)	d_{32} (mm)	$\hat{\sigma}$ (mm)	d_{00} (mm)	Err
D16	50	3.18	0.90	3.42	3.31	3.68	0.27	3.07	0.138
D18	50	3.75	0.79	3.92	3.41	4.08	0.20	3.68	0.078
D21	50	2.45	0.52	2.56	2.26	2.67	0.21	2.40	0.081
D24	50	2.84	0.58	2.96	2.59	3.09	0.20	2.78	0.133
D3	49	5.48	2.18	6.29	6.75	7.16	0.36	5.18	0.092
E14	96	3.12	0.81	3.32	3.03	3.53	0.25	3.03	0.092
E16	101	4.48	1.17	4.77	4.39	5.07	0.25	4.35	0.066
E17	50	4.80	1.50	5.27	5.60	5.79	0.31	4.56	0.095
E23	18	3.46	0.67	3.59	3.06	3.72	0.19	3.40	0.042
E24	50	3.41	0.89	3.63	3.28	3.84	0.24	3.32	0.056
E7	96	5.82	2.75	7.03	8.14	8.42	0.42	5.37	0.102
G17	35	4.73	0.58	4.79	3.44	4.86	0.12	4.69	0.044
G29	76	3.81	0.77	3.96	3.28	4.11	0.19	3.75	0.113
G26	50	2.99	0.77	3.18	2.95	3.38	0.24	2.91	0.059
G21	50	3.09	0.56	3.19	2.48	3.28	0.17	3.06	0.150
I17	50	3.28	0.70	3.42	2.97	3.57	0.21	3.21	0.079
H23	50	3.44	0.91	3.68	3.70	3.94	0.26	3.31	0.054
I18	50	3.73	0.74	3.87	3.30	4.02	0.19	3.66	0.059

Table 6
Bubble diameters at pipe outlet

Run	k	d_{10} (mm)	σ_{10} (mm)	d_{30} (mm)	σ_{30} (mm)	d_{32} (mm)	$\hat{\sigma}$ (mm)	d_{00} (mm)	Err
D16	103	6.59	2.80	7.69	8.29	8.87	0.38	6.20	0.106
D18	102	8.74	4.15	10.62	12.44	12.80	0.43	8.02	0.082
D21	50	4.23	1.28	4.61	4.64	5.02	0.29	4.06	0.079
D24	100	5.62	1.87	6.24	6.63	6.92	0.32	5.34	0.078
D3	21	23.31	5.34	24.35	19.96	25.31	0.20	22.98	0.209
E14	125	7.20	2.62	8.06	8.16	8.94	0.32	6.91	0.192
E16	100	9.97	4.08	11.45	11.70	12.94	0.35	9.53	0.115
E17	98	10.62	5.64	13.26	14.96	16.18	0.45	9.84	0.108
E23	32	4.97	1.05	5.18	4.42	5.39	0.20	4.88	0.113
E24	126	6.02	2.52	7.04	8.06	8.19	0.39	5.60	0.099
E7	16	21.09	5.59	22.27	18.33	23.28	0.21	20.84	0.374
G17	45	6.73	1.82	7.20	6.77	7.68	0.25	6.53	0.135
G29	105	9.18	5.04	11.54	13.12	14.05	0.44	8.60	0.225
G26	100	5.97	3.07	7.34	8.05	8.78	0.42	5.60	0.187
G21	148	6.90	3.13	8.30	10.28	9.96	0.43	6.31	0.059
I17	100	8.50	3.62	10.01	11.44	11.75	0.40	7.87	0.091
H23	100	8.66	3.54	9.99	10.64	11.41	0.36	8.19	0.125
I18	100	9.40	4.59	11.54	13.56	14.07	0.45	8.57	0.098

geometric and volumetric diameters, the parameters of the log-normal law $d_{00}, \hat{\sigma}$ and the error Err.

It is important to mention that no bubble break-up has been observed in these experiments, which explains the high values of the bubble sizes found at the pipe outlet. This result is in agreement with a previous study of Risso and Fabre (1998) on bubble break-up in a turbulent field in microgravity. The authors have found that break-up of bubble of diameter d only appears for a critical Weber number $We_{\text{crit.}}$ greater than 4.5 with

$$We_{\text{crit.}} = \frac{\rho_L V_t^2 d}{\sigma},$$

where V_t being a velocity scale characteristic of the turbulence defined by $V_t^2 \approx 2(\varepsilon d)^{2/3}$ and ε is the dissipation rate of turbulent kinetic energy. In our experiments ε is estimated at the pipe centre (63), where the bubbles are mostly present, in function of the integral length scale of turbulence l_e and the friction velocity u_*. u_* is deduced from the pressure drop measurement (61) and l_e is estimated from (59). The critical Weber number is always much smaller than one in the experiments.

6. Simulations of the bubble sizes evolution along a pipe in microgravity

In bubbly pipe flow under microgravity conditions no bubble break-up is observed and the changes in bubble size due to mass transfer or pressure variation are negligible. Therefore the growth rate G can be put equal to zero and (7) simplifies to

$$\frac{\partial S_\gamma}{\partial t} + \nabla \cdot \left(\mathbf{v}_\gamma S_\gamma\right) = \varphi_\gamma \tag{52}$$

the source term φ_γ being only due to coalescence. Here we approximate the bubble velocity as being independent of bubble size and determined only by the radial position of the bubble in the tube, so that $\mathbf{v}_\gamma = \mathbf{v}_G$ for all γ. This is a reasonable approximation for developed bubbly pipe flow under microgravity because of the absence of buoyancy.

In this work, Eq. (52) is further simplified, assuming a steady, quasi-parallel pipe flow. The transport equation then reduces to a one-dimensional ordinary differential equation in axial pipe co-ordinate z

$$\frac{\mathrm{d}}{\mathrm{d}z}\left(V_G S_\gamma\right) = \varphi_\gamma, \tag{53}$$

where V_G being the axial mean velocity of the gas. The effect of turbulence is thus neglected except in relation to the source term, φ_γ, which derives from turbulence-driven collisions. The bubble concentration and bubble-diameter distribution are determined by ensemble averaging. In addition, the pressure drop Δp over the tube length is small compared with the inlet pressure $p_0, \Delta p \ll p_0$, and the influence of the gas compressibility on the gas velocity V_G can therefore be neglected. (53) now yields

$$V_G \frac{\mathrm{d}S_\gamma}{\mathrm{d}z} = \varphi_\gamma. \tag{54}$$

Substituting (45) in (54) for $\gamma = 1$ and $\gamma = 2$, the following system of linear ordinary differential equations is obtained for the moments S_1 and S_2

$$\frac{dS_1}{dz} = K_c\left(\frac{8\pi}{3}\right)^{1/2}\left(\frac{6\alpha}{\pi}\right)^{2/3}\frac{C_t\varepsilon^{1/3}}{\sqrt{1.61}V_G}\left(2^{1/3}-2\right)S_1^{4/3}f(1,\hat{\sigma},P_{00}), \tag{55}$$

$$\frac{dS_2}{dz} = K_c\left(\frac{8\pi}{3}\right)^{1/2}\left(\frac{6\alpha}{\pi}\right)^{1/3}\frac{C_t\varepsilon^{1/3}}{\sqrt{1.61}V_G}\left(2^{2/3}-2\right)S_2^{5/3}f(2,\hat{\sigma},P_{00}). \tag{56}$$

Discretizing the derivative on the LHS by means of a first-order Euler scheme, (55) and (56), can be solved numerically, after modelling of the mean gas velocity V_G, the coefficient C_t and the dissipation rate of the turbulent kinetic energy ε.

For flow under microgravity conditions, the mean gas velocity V_G can be estimated using the drift flux model (Zuber and Findlay, 1965; Colin et al., 1991):

$$V_G = \frac{j_G}{\alpha} = \frac{C_0}{1-C_0\alpha}j_L, \tag{57}$$

where j_L is the superficial liquid velocity, j_G the superficial gas velocity, α is the cross-sectional average of the gas fraction, and C_0 is a coefficient depending on the radial distributions of void fraction and liquid velocity. An experimental value of 1.2 has been found for C_0 in microgravity pipe flows (Colin et al., 1991). Experimental data (Kamp, 1996) show that the radial gas fraction distribution under microgravity conditions is rather flat in the centre of the pipe, but decreases near the wall. In the following we will assume that the gas fraction distribution is constant in the pipe section: $\alpha = \alpha_c$ where α_c is the gas fraction in the centre of the pipe. This is a reasonable approximation, although the real situation is probably somewhere between a uniform gas fraction and a centre peaking gas fraction distribution as assumed by Colin et al. (1996).

In the case of bubbly flow under microgravity conditions, the sources of collision due to different bubble slip velocities, wake interactions or helicoïdal/zigzag motion are not present because of the absence of buoyancy. For the conditions under which the experiments were carried out, the flow is turbulent and the radial variation of the axial liquid velocity u is to a reasonable approximation given by a power law

$$u = u_{axis}(1-2r/D)^{1/n}, \tag{58}$$

where r indicates the radial position in the tube, u_{axis} the liquid velocity on the pipe axis and n is a constant, $n \approx 7$ (Schlichting, 1979). The local axial bubble velocity is also given to (58) to the first approximation, buoyancy being absent. Since this distribution is very flat, the source of bubble collision due to motion in mean velocity gradients, will also be even smaller than under terrestrial conditions (where it is typically much smaller than the turbulence-induced motion for high flow Reynolds numbers) and may be neglected.

In order to estimate whether the collisions can be induced by large eddies in the pipe flow, the integral length scale l_e of turbulence has to be estimated. This scale is approximately given by (Hinze, 1975)

$$l_e = \frac{\kappa D}{2}, \tag{59}$$

where κ is the von Karman constant, $\kappa = 0.41$. For $D = 4$ cm, $l_e = 8$ mm, so that a bubble diameter of 8 mm constitutes the upper limit at which the model is applicable.

The modelling of the coefficient C_t is still subject to discussion (Eppinger, 1995; Kamp, 1996). C_t is the ratio between the dispersed phase velocity fluctuations and the continuous phase velocity fluctuations. The most common modelling is based on transforming the momentum equation of the bubble to the frequency domain, based on the approach of Hinze (1975). The crossing trajectories effect (Deutsch, 1992) is expected to be weak in the absence of a relative velocity of the bubbles. Under this approximation, C_t can be estimated by

$$C_t^2 = \frac{9 + 72\beta v_L l_e/d^2 u'}{1 + 72\beta v_L l_e/d^2 u'}, \tag{60}$$

where the coefficient β is taken equal to 0.6, v_L is the kinematic viscosity of the liquid, and u' is the r.m.s value of the axial liquid velocity. It is assumed that C_t is only weakly dependent on bubble size and the diameter d is set equal to d_{00}. The turbulent velocity scale u' is a function of the radial position of the bubble in the pipe. An estimation of u' is given by the friction velocity u_*. u_* can either be determined experimentally from measurement of the pressure gradient $\mathrm{d}p/\mathrm{d}z$ in the pipe flow

$$u_* = \sqrt{-\frac{D}{4\rho_L}\frac{\mathrm{d}p}{\mathrm{d}z}} \tag{61}$$

or it can be estimated from Blasius′ equation, which gives a good approximation of the wall shear stress in microgravity bubbly pipe flows (Colin et al., 1991)

$$u_* = (j_L + j_G)\sqrt{\frac{0.079Re^{-1/4}}{2}} \quad \text{with } Re = \frac{j_L + j_G}{v_L}D, \tag{62}$$

where Re being a mixture Reynolds number.

The rate of dissipation of the turbulent kinetic energy ε can be estimated using the integral length scale of turbulence l_e, and the turbulent velocity of the liquid phase in the pipe centre $u' \approx u_*$

$$\varepsilon \approx \frac{u'^3}{l_e} \approx \frac{2u_*^3}{\kappa D}. \tag{63}$$

In order to compare the experimentally observed coalescence behaviour to that predicted by the model that was presented, Eqs. (55) and (56) are numerically solved. For the estimation of the friction velocity, (61) is applied, using the experimentally measured pressure gradient. The boundary conditions for the simulations are obtained by using the values of d_{00} and $\hat{\sigma}$ that were determined from the flow visualizations at the pipe inlet (see Table 5). These values are used in Eq. (10) to calculate S_1 and S_2 at the pipe inlet.

From the calculated axial variation of S_1 and S_2 that follow from the simulations, the axial variation of d_{00} and $\hat{\sigma}$ is calculated from (47). In Fig. 6, the predicted values of $d_{00}, \hat{\sigma}$, and the Sauter diameter d_{32} at the pipe outlet are plotted versus the experimentally obtained values of these parameters. From a fitting procedure, it followed that the best agreement was obtained using the values $K_c = 1$ and $K_p = 2$, which indeed prove to be of order one, as it was anticipated.

For most of the runs the model is in good agreement with the experimental data. The discrepancy between prediction and experimental results observed for the runs E7 and D3 is due to the fact that for these cases large bubbles are observed. The hypothesis of turbulence driven

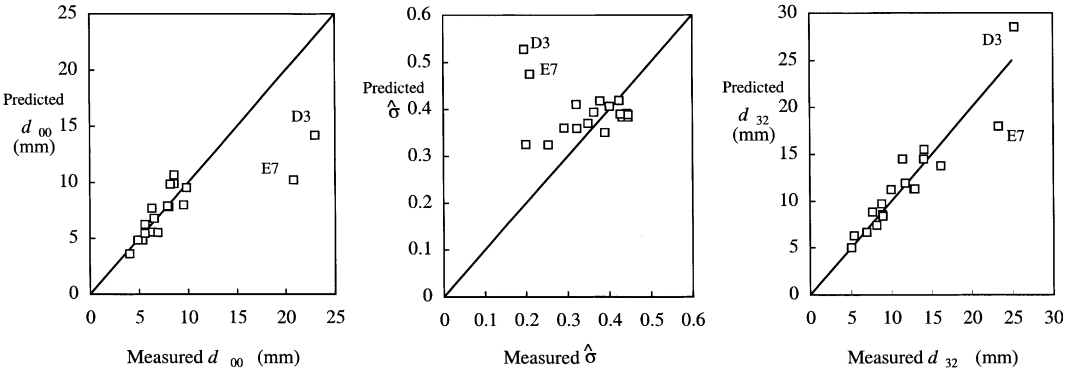

Fig. 6. Comparison of predicted and experimental values of $d_{00}, \hat{\sigma}$ and d_{32}.

collision of particles with diameter smaller than the integral length scale of turbulence ($l_e = 8$ mm) is then no longer valid.

7. Parameter study

Given the success of the coalescence model in predicting the observed coalescence behaviour, it interesting to conduct a number of numerical experiments to investigate the influence of the system parameters. Taking the best-fit values of the model constants determined in the previous section ($K_c = 1$ and $K_p = 2$), the model is used to study the influence of three principal parameters on the coalescence rate:

1. the cross-sectional averaged gas volume fraction α;
2. the superficial liquid velocity j_L or, equivalently, the rate of dissipation of turbulent kinetic energy ε;
3. the characteristic bubble diameter $d_{00,in}$ at the pipe inlet.

The rate of coalescence is characterized by the relative increase in Sauter diameter $d_{32}/d_{32,in}, d_{32,in}$ being the Sauter diameter at the pipe inlet. The numerical simulations are carried out for a pipe of 40 mm diameter and 3 m length. The superficial liquid velocities are varied between 0.2 and 2 m/s, the mean gas fraction between 0.02 and 0.15 and the bubble characteristic diameter at the inlet between 1 and 8 mm.

The dependence of the coalescence rate on the initial size-distribution width, $\hat{\sigma}$, is not examined in detail in most of practically relevant cases of bubbly pipe flow $\hat{\sigma}$ lies within a relatively narrow range: between 0.15 and 0.25. In addition, the influence of the initial $\hat{\sigma}$-value on the coalescence rate proved to be minor: for the reference case of $j_L = 1$ m/s, $\alpha = 0.05$ and $d_{00,in} = 3$ mm, the predicted relative increases in the Sauter diameter varies between 2.00 and 2.54 as $\hat{\sigma}$ values between 0.15–0.4. In the remaining simulations the initial value of $\hat{\sigma}$ is held constant at 0.25.

7.1. Evolution of coalescence with distance along the pipe

The evolution of the characteristic diameter d_{00} and the width parameter $\hat{\sigma}$ has been computed for a pipe of 3 m length, a superficial liquid velocity $j_L = 1$ m/s and two different values of the

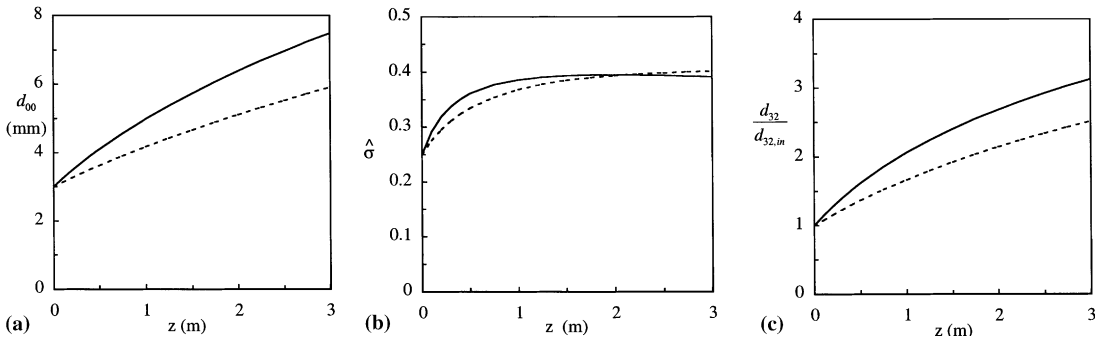

Fig. 7. Longitudinal evolution of the characteristic diameter, the width parameter and the Sauter diameter for two mean void fraction values: —— $\alpha = 0.1$ and - - - - $\alpha = 0.05$.

mean gas volume fraction α. The results are plotted in Fig. 7. The diameter d_{00} (Fig. 7(a)) increases along the axial pipe co-ordinate, somewhat faster near the pipe inlet than near the outlet. As would be expected, the diameter increases more rapidly for the higher gas fraction since the collision rate of a given bubble is proportional to α.

The width parameter $\hat{\sigma}$ (Fig. 7(b)) also increases rapidly at first but approaches an asymptotic value. Coalescence leads to a broadening of the pdf of bubble diameters. Larger bubbles appear due to coalescence while small bubbles remain present in the flow. From Fig. 4(a) it is clear that coalescence is still significant near the pipe outlet, while at the same time the width of the pdf no longer increases. This can be explained by the fact that small bubbles have a greater probability of coalescing than the larger ones, so that at some point equilibrium is reached between coalescence of large bubbles and coalescence of small bubbles. At that point the result of bubble coalescence on the pdf is merely a shift towards larger diameters.

The relative increase in Sauter diameter along the axial co-ordinate (Fig. 7(c)) shows a similar tendency to that observed for the diameter d_{00}.

7.2. Dependence of coalescence on gas volume fraction

The predicted influence of the gas volume fraction on the coalescence rate is displayed in Fig. 8. The relative increase in the Sauter diameter over a length of 3 m, $d_{32}/d_{32,\mathrm{in}}$, is plotted versus the gas volume fraction for different values of the liquid velocity, taking $d_{00,\mathrm{in}} = 3$ mm (Fig. 8(a)) and for various values of $d_{00,\mathrm{in}}$ and a given liquid velocity $j_{\mathrm{L}} = 1$ m/s (Fig. 8(b)). The solid line in the two figures corresponds to the same case ($j_{\mathrm{L}} = 1$ m/s and $d_{00,\mathrm{in}} = 3$ mm). The simulations are run in the range of validity of the model ($d_{00} < l_{\mathrm{e}}$) which limits the ranges of the curves in the Figs. 8 and 9.

Fig. 8(a) shows that for a gas volume fraction smaller than 0.03, the relative Sauter diameter increases approximately linearly with gas volume fraction. At higher gas volume fraction the increase of relative Sauter diameter with increasing gas volume fraction becomes slower. The Sauter diameter increase between pipe inlet and outlet is larger for low liquid flow rates and for smaller bubble sizes at the injection point. A qualitative explanation of these results is provided in Sections 7.3 and 7.4.

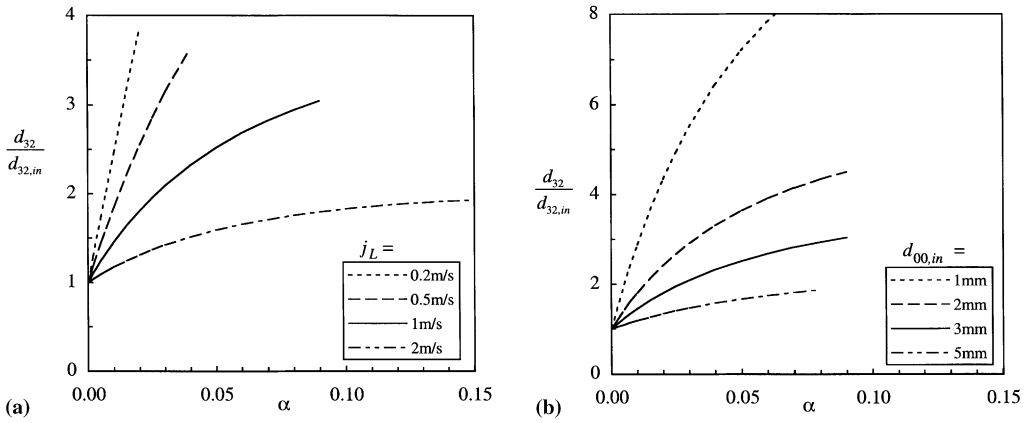

Fig. 8. Influence of the mean void fraction upon the relative increase in the Sauter diameter at the pipe outlet $L = 3$ m: (a) $d_{00,\mathrm{in}} = 3$ mm and (b) $j_{\mathrm{L}} = 1$ m/s.

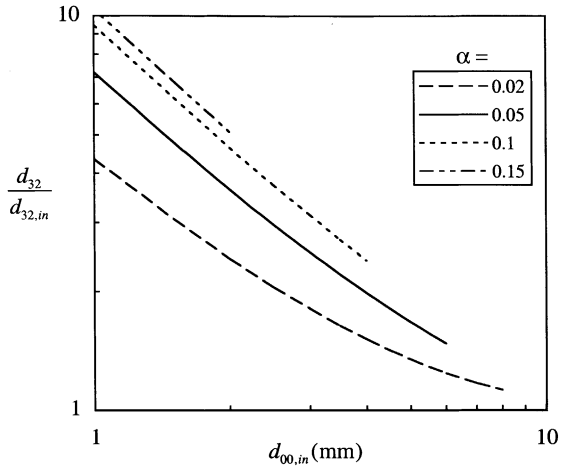

Fig. 9. Influence of the characteristics inlet diameter upon the relative increase in the Sauter diameter for $j_{\mathrm{L}} = 1$ m/s.

7.3. Dependence of coalescence on liquid flow rate

The influence of the superficial liquid velocity j_{L} on the relative increase in Sauter diameter is threefold. An increasing liquid flow rate:

- diminishes the residence time of the bubbles inside the pipe;
- decreases the coalescence probability because of an increase in the Weber number, via an increase in ε;
- increases the collision rate through an increase of the dissipation rate of turbulent kinetic energy, ε;

To the first approximation the first and third effects compensate each other [8] and the second effect accordingly dominates (Fig. 8(a)). A similar result was obtained experimentally in vertical flows in the presence of gravity where coalescence rates were observed to be much lower than under microgravity conditions despite higher collision rates as a result of increased relative bubble velocities (Kamp, 1996).

7.4. Dependence of coalescence on the bubble diameter

The influence of the mean bubble diameter $d_{00,\mathrm{in}}$ at the pipe inlet on the relative increase in Sauter diameter at the pipe outlet in shown in Fig. 9 for a pipe length of 3 m and a superficial liquid velocity of 1 m/s. Bubble size proves to be an important parameter in the coalescence rate: small bubbles tend to coalesce much more than large bubbles. The ratio $d_{32}/d_{32,\mathrm{in}}$ is approximately inversely proportional to a power of $d_{00,\mathrm{in}}$.

8. Conclusions

The model developed involves two steps, which are essentially separable. In the first, the expressions put forward earlier for the collision frequency and coalescence probability of equal bubbles during turbulence-driven, high-Reynolds-number collisions (Chesters, 1991) are extended to unequal bubbles and to take account of bubble–turbulence and bubble–bubble interactions. In the second, the resulting expression for the coalescence rate is used to derive source terms in the transport equations for the moment densities, S_j, which can readily be evaluated locally within a CFD code. The result is an extremely compact framework capable of providing predictions of the evolution of bubble size distributions in space and time at the expense of only two additional scalar transport equations. The predictions of the model are compared with experimental data obtained in cases in which the collisions between bubbles are only turbulence induced. This condition has been satisfied in bubbly pipe flows under microgravity conditions for which data concerning the evolution of bubble diameter distribution along the pipe are presented. The model assumes the bubbles to be almost spherical and smaller than the integral length scale of turbulence, l_e, while collisions are assumed to arise primarily from liquid turbulence. In the microgravity pipe flows concerned the approximation of spherical bubbles proves acceptable up to bubble diameters of 20 mm. The requirement that $d < l_e$ is more restrictive, l_e being around 8 mm. The model includes two unknown constants of order unity which represent approximations that were made in the development of the model. Comparing the model predictions with the experimental data, the following values for these constants were obtained: $K_c = 1$ and $K_p = 2$. Using these values, the model is capable of predicting bubble size pdf at the pipe outlet over the investigated range of liquid flow rate, gas flow rate and bubble size pdf at injection.

To survey the global trends predicted by the model a parametric study has been conducted. An important result of this study is the prediction that bubble growth due to coalescence between

[8] Ignoring the weak Re-dependence of u_*, and bearing in mind that $j_G \ll j_L$, (62) indicates that u_* and hence (via (35), (36) and (63)) the collision rate varies as j_L whereas the residence time varies as $1/j_L$. To the first approximation, therefore, the collision rate per unit axial distance for a given bubble size is almost independent of j_L.

inlet and outlet diminishes with increasing liquid flow rate, due primarily to a reduction coalescence probability arising from an increase in collision velocities.

The successful prediction of coalescence in pipe flows under microgravity conditions is an important step toward a complete understanding of the evolution of bubble size in these flows (better prediction of the transition to slug flow) but also in more complex flows where gravity plays an important role. Indeed, in presence of buoyancy, the coalescence mechanisms are much harder to model because the velocity difference between bubbles of different sizes is another source of bubble collisions. In vertical upward flow the bubbles are furthermore concentrated in regions of high velocity gradients. Likewise, incorporation of the influence of surfactant is straightforward, given models for their effect on film drainage. These effects add to that of turbulence, which has been clearly highlighted in the present microgravity experiments.

Acknowledgements

The authors would like to thank the European Community (Brite Euram Project BE 4096) for funding and the Centre National d'Etudes Spatiales for financial support and organization of the parabolic flights campaigns.

Appendix A. Relative contributions of turbulence and mean-flow velocity gradients to bubble collision velocities

The starting point for an estimation of bubble collision velocities is the velocity variation in the continuous phase over a distance, l, of the order of $(d_1 + d_2)/2$. The order of magnitude of the contribution of inertial-subrange turbulence to this velocity variation, V_{turb}, is given by (34):

$$V_{\text{turb}} \sim (\varepsilon \ell)^{1/3}. \tag{A.1}$$

The corresponding contribution, V_{mean}, of mean-velocity variation is given by

$$V_{\text{mean}} \sim (V/L)\ell, \tag{A.2}$$

where V and L denote a characteristic system velocity and length scale. For large system Reynolds numbers ε is furthermore related to V and L by

$$\varepsilon = kV^3/L, \tag{A.3}$$

where k depends on the system geometry, varying from order 10^{-3} for wall-bounded flows to order 10^{-1} for free flows. Combination of (A.1)–(A.3) now yields

$$\frac{V_{\text{turb}}}{V_{\text{mean}}} \approx k^{1/3}\left(\frac{L}{l}\right)^{2/3}. \tag{A.4}$$

In most high Reynolds number industrial systems, such as stirred tanks, L is two or more orders of magnitude larger than l and the influence of mean velocity gradients should be minor. In the experiments reported in Section 5, this approximation is poorer although in the centre region of the tube where most of the bubbles can be found, the velocity is almost homogeneous so that (A.2) considerably overestimates V_{mean}.

Appendix B. Bubble entrapment in vortices

Consider a vortex whose centre travels at the mean velocity of the liquid. The centripetal acceleration of the liquid within the vortex is of order U_v^2/L_v where U_v and L_v denote the velocity and length scales of the vortex. The centripetal acceleration of a bubble located within the vortex will be therefore of order $3U_v^2/L_v$. [9] On entering the vortex, the velocity of the bubble relative to the vortex centre will be the sum of its mean velocity, U, relative to the liquid and its fluctuating velocity $C_t V_{turb}$. As these velocities are uncorrelated, their average magnitude will be $[U^2 + (C_t V_{turb})^2]^{1/2}$ and the centripetal acceleration of the bubble will be given by $[U^2 + (C_t V_{turb})^2]/R_c$, where R_c denotes the radius of curvature of the bubble trajectory. Equating these two expressions for the centripetal acceleration of the bubble we obtain

$$[U^2 + (C_t V_{turb})^2]/R_c = 3U_v^2/L_v. \tag{B.1}$$

For bubble entrapment to occur R_c must be smaller than the radius of the vortex

$$R_c < L_v/2. \tag{B.2}$$

From (B.1) and (B.2) the criterion for entrapment is thus

$$U^2 + (C_t V_{turb})^2 < 3U_v^2/2. \tag{B.3}$$

If the vortex corresponds to an energy-containing eddy, $U_v = V_{turb}$ and (B.3) becomes

$$(U')^2 + C_t^2 < 3/2, \tag{B.4}$$

where U' denotes the ratio U/V_{turb}. In the present experimental study gravity is absent and U' is negligible so that (B.4) reduces to $C_t^2 < 3/2$. The measured C_t-values were, however, much larger than unity so that entrapment is not expected, nor was it observed. In most practical systems involving large bubble Reynolds numbers U is of the order of 10^{-1} m/s or more and U' of the order of unity. Since $C_t \geqslant 1$, (B.4) is then automatically satisfied.

For eddies/vortices either smaller or larger than the energy-containing eddies, $U_v < V_{turb}$ and (B.3) is satisfied even more readily.

References

Abid, S., Chesters, A.K., 1994. The drainage and rupture of partially-mobile films between colliding drops at constant approach velocity. Int. J. Multiphase Flow 20, 613–629.

Achard, J.L., 1978. Contribution à l'étude théorique des écoulements diphasiques en régime transitoire. Ph.D. Thesis de l'Université Scientifique et Médicale et de l'Institut National Polytechnique de Grenoble, France.

Bongiovanni, C., 1996. Traitement d'image appliqué à la mesure de la taille, de la vitesse et de la déformation des bulles. Ph.D. Thesis, Institut National Polytechnique de Toulouse, France.

Chesters, A.K., Hofman, G., 1982a. Bubble coalescence: the inertia controlled, low Weber number case. Technical Report, Laboratory of Aero- and Hydrodynamics, Delft University of Technology, The Netherlands.

[9] Because its virtual mass is half that of the liquid displaced, a bubble suddenly subjected to an acceleration of the surrounding liquid accelerates twice as fast. With respect to the reference frame its acceleration is therefore three times that of the liquid.

Chesters, A.K., Hofman, G., 1982b. Bubble coalescence in pure liquids. Appl. Sci. Res. 38, 353–361.
Chesters, A.K., 1991. The modelling of coalescence processes in fluid-liquid dispersions – a review of current understanding. Trans. I. Chem. E 69 (part A), 353–361.
Colin, C., 1990. Ecoulements diphasiques à bulles et de poches en micropesenteur. Ph.D. Thesis, Institut National Polytechnique, Toulouse, France.
Colin, C., Fabre, J., Dukler, A., 1991. Gas liquid flow at microgravity conditions – I (Dispersed bubble and slug flow). Int. J. Multiphase Flow 17, 533–544.
Colin, C., Fabre, J., Mc Quillen, J., 1996. Bubble and slug flow at microgravity conditions: state of Knowledge and open questions. Chem. Eng. Comm. 141–142, 155–173.
Coulaloglou, C.A., Tavlarides, L.L., 1977. Description of interaction processes in agitated liquid–liquid dispersions. Chem. Eng. Sci. 32, 1289–1297.
Deutsch, E., 1992. Dispersion de particles dans une turbulence isotrope stationnaire calculée par simulation numérique directe des grandes échelles. Ph.D. Thesis, Ecole Centrale de Lyon, France.
Duineveld, P.C., 1994. Bouncing and coalescence of two bubbles in water. Ph.D. Thesis, University of Twente, The Netherlands.
Eppinger, K., 1995. Etude du mouvement des bulles dans un turbulence homogène isotrope. Ph.D. Thesis, Institut National Polytechnique, Toulouse, France.
Heng-Kwong, T., Koch, D., 1994. Collisions of slightly deformable, high Reynolds number bubbles with short-range repulsive forces. Phys. Fluids 6, 2591–2605.
Hill, D.H., 1998. The computer simulation of dispersed two-phase flows. Ph.D. Thesis, University of London, Imperial College of Science, Technology and Medicine, England.
Hinze, J.O., 1975. Turbulence – An Introduction to its Mechanisms and Theory. McGraw-Hill, New York.
Kamp, A.M., 1996. Ecoulements turbulents à bulles dans une conduite en micropesanteur. Ph.D. Thesis, Institut National Polytechnique, Toulouse, France.
Kamp, A.M., Colin, C., Fabre, J., 1995. The local structure of turbulent bubbly pipe flow under different gravity conditions. In: Proceedings of the Second International Conference on Multiphase Flow. Kyoto.
Kirkpatrick, R.D., Lockett, M.J., 1974. The influence of approach velocity on bubble coalescence. Chem. Eng. Sci. 29, 2363–2373.
Kuboi, R., Komosawa, I., Otake, T., 1972. Collision and coalescence of dispersed drops in turbulent liquid flow. J. Chem. Eng. Jpn. 5, 423–424.
Lamb, H., 1932. Hydrodynamics, 6th. Cambridge University Press, Cambridge.
Lee, J., Hodgson, T.D., 1968. Film flow and coalescence – I. Basic relations, film shape and criteria for interface mobility. Chem. Eng. Sci. 23, 1375–1397.
Moore, D.W., 1963. The boundary layer on a spherical gas bubble. J. Fluid Mech. 16, 161–176.
Piret, J.J., 1980. Etude des effects de la coalescence des bulles sur les écoulements de gaz en lit fluidisé. ''Doctorat d'Etat'' thesis, Université Pierre et Marie Curie, Paris, France.
Randolph, A.D., Larson, M.A., 1971. Theory of Particulate Processes. Academic Press, New York.
Risso, F., Fabre, J., 1998. Oscillations and break-up of a bubble immersed in a turbulent field. J. Fluid Mech. 372, 323–355.
Ross, S.L., 1971. Measurements and models of dispersed phase mixing process. Ph.D. Thesis, University of Michigan, USA.
Schlichting, H., 1979. Boundary Layer Theory. McGraw-Hill, New York.
Svendsen, H.F., Luo, H., 1996. Modeling of approach processes for equal or unequal sized particles. Can. J. Chem. Eng. 14, 321–330.
Zuber, N., Findlay, J.A., 1965. Average volumetric concentration in two-phase systems. J. Heat Transfer 87, 453–468.